Available online at www.sciencedirect.com

ScienceDirect

Underground Space 23 (2025) 89–112

www.keaipublishing.com/undsp

Research Paper

Interpretation of an artificial ground freezing field trial at Fori Imperiali in Rome

Giulia Guida [a,*], Arianna Pucci [a], Eliano Romani [b], Giulia M.B. Viggiani [c], Francesca Casini [a]

[a] *Università di Roma Tor Vergata, Rome 00133, Italy*
[b] *Metro C S.c.p.A., Rome 00172, Italy*
[c] *University of Cambridge, Cambridge CB21PZ, United Kingdom*

Received 30 September 2024; received in revised form 15 November 2024; accepted 23 December 2024
Available online 11 April 2025

Abstract

This paper describes a field trial of artificial ground freezing (AGF) carried out in connection with the construction of Line C of Roma underground. AGF was one of the options considered for the temporary stabilisation of the ground during the excavation of Colosseo-Fori Imperiali Station. The field trial aimed at assessing the feasibility of AGF in the complex soil profile and groundwater regime of the subsoil of the historical centre of Roma by establishing the response of the subsoil to the imposed freezing loads, the ability to create a continuous frozen wall, and the associated coolant consumption. The extensive monitoring data were exploited to conduct a detailed analysis of the transient freezing process in the stratified subsoil and used to develop and validate a three-dimensional thermo-hydraulic numerical model. Special attention was given to defining and applying appropriate boundary conditions at the freezing pipes. The paper discusses the main factors affecting the time-dependent freezing process and explores the applicability of simplified two-dimensional models for the Fori Imperiali AGF field trial.

Keywords: Tunnelling; Artificial ground freezing; Numerical modelling; Heat transfer

1 Introduction

Artificial ground freezing (AGF) is used in underground construction to improve the stability of the ground and control the groundwater flow during excavation. The technique consists of driving freeze pipes into the ground and then circulating a refrigerating medium until the ground temperature around the pipes is below the freezing point of the groundwater. The resulting frozen ground exhibits improved mechanical and hydraulic properties, temporarily supporting the excavation and preventing groundwater inflow.

The most commonly used refrigerating media are nitrogen (N_2), liquid at about −196 °C and then exhaust in the atmosphere (open circuit freezing), or a solution of calcium chloride ($CaCl_2$) in water (brine), inserted in the pipes at −20 to −40 °C and re-circulated through a refrigeration plant (closed circuit freezing) (Orth & Muller, 2013; Alzoubi et al., 2020). Compared to brine, the advantages of nitrogen freezing include a more straightforward site setup and significantly lower temperatures, enabling a faster achievement of the target frozen body and better handling of emergencies. However, nitrogen freezing comes with much higher operating costs than brine freezing, which is generally preferable for more extensive and long-term freezing applications. Braun et al. (1979), Jessberger (1980), Schmall and Braun (2006), and Chang and Lacy

* Corresponding author.
E-mail address: giulia.guida@uniroma2.it (G. Guida).
Peer review under the responsibility of Tongji University

https://doi.org/10.1016/j.undsp.2024.12.006

Nomenclature

A_{ann}	outer annulus area of the pipe (m^2)
$c\prime$	effective cohesion (kPa)
$c_{p,i}$	specific heat capacity of ice ($J/(kg \cdot K)$)
$c_{p,N}$	specific heat capacity of nitrogen ($J/(kg \cdot K)$)
$c_{p,s}$	specific heat capacity of solid grains ($J/(kg \cdot K)$)
$c_{p,w}$	specific heat capacity of unfrozen water ($J/(kg \cdot K)$)
C_w	water capacity (1/kPa)
d_c	external diameter of the perforation hole (m)
$d_{p,eq}$	equivalent diameter of the outer pipe annulus (m)
$d_{p,in}$	external diameter of the inner pipe (m)
$d_{p,out}$	external diameter of the outer pipe (m)
d_s	diameter of affected soil (m)
$d_{s,f}$	diameter of the steady state threshold between the frozen and unfrozen affected soil (m)
E_i	internal energy of ice (J/K)
E_s	internal energy of solid grains (J/K)
E_w	internal energy of unfrozen water (J/K)
g	gravity acceleration (m/s^2)
G_0	small strain shear modulus (kPa)
h_N	convection heat transfer coefficient ($W/(m^2 \cdot K)$)
$\boldsymbol{i}_c$	conductive heat flux (W/m^2)
I_p	plasticity index
$\boldsymbol{j}_{Ew}$	convective heat flux
k_{rel}	relative permeability function
$\boldsymbol{k}_{sat}$	saturated hydraulic conductivity tensor (m/s)
$\boldsymbol{K}$	unfrozen hydraulic conductivity tensor (m/s)
L	water latent heat of fusion (J/K)
L_p	pipe length (m)
m	van Genuchten parameter
$\dot{m}_N$	mass rate of nitrogen (kg/s)
M	initial slope of the temperature variation with time (K/s)
p_i	pressure of the ice (kPa)
p_w	pressure of the unfrozen water (kPa)
P	van Genuchten parameter (kPa)
Pr	Prandtl number
Q	heat (J)
$\dot{Q}$	thermal power per unit length (W/m)
$R_{1,fluid}$	thermal resistance of the convection process between coolant and pipe (m·K/W)
$R_{2,pipe}$	thermal resistance of the conduction process across the pipe tube (m·K/W)
$R_{3,insul}$	thermal resistance of the conduction process across the insulation cover (m·K/W)
$R_{4,mortar}$	thermal resistance of the conduction process across the mortar (m·K/W)
$R_{5,soil}$	thermal resistance of the conduction process across the soil (m·K/W)
$R_{5,SG}^{frozen}$	hermal resistance of the conduction process across the frozen SG layer (m·K/W)
$R_{5,Tb1a}^{frozen}$	thermal resistance of the conduction process across the frozen Tb1a layer (m·K/W)
$R_{5,SG}^{unfrozen}$	thermal resistance of the conduction process across the unfrozen SG layer (m·K/W)
$R_{5,Tb1a}^{unfrozen}$	thermal resistance of the conduction process across the unfrozen Tb1a layer (m·K/W)
R_{SG}	overall thermal resistance in the SG layer (m·K/W)
R_{Tb1a}	overall thermal resistance in the Tb1a layer (m·K/W)
R_i	thermal resistance of the *i*-layer (m·K/W)
Re	Reynolds number
s	suction (kPa)
s_u	undrained strength (kPa)
S	storage term (1/kPa)
S_i	ice water degree of saturation
S_{res}	residual unfrozen degree of saturation
S_w	unfrozen water degree of saturation
t	time (s)
t_i	thickness of the insulation elastomer (m)
$t_{p,in}$	thickness of the inner freezing pipe (m)
$t_{p,out}$	thickness of the outer freezing pipe (m)
T	temperature (K)
T_f	temperature of the circulating fluid (K)
$T_{f,in}$	inlet temperature of the circulating fluid (K)
T_p	temperature at the boundary of the freezing pipes (K)
T_p^{∞}	steady state temperature at the boundary of the freezing pipes (K)
T_s	surface temperature of the outer tube (K)
T_0	undisturbed soil temperature (K)
$\boldsymbol{u}$	velocity of the unfrozen water (m/s)
V_N	average velocity of nitrogen (m/s)
w	water content
w_L	liquid limit
x_p	length coordinate of the pipe (m)
z	the vertical coordinate (m)
$\Delta T_{coolant-soil}$	variation of temperature at the boundary with the soil (K)
γ	specific unit weight of soil (kN/m^3)
λ_{eq}	equivalent thermal conductivity for the multi-phase soil (W/(m·K))
λ_i	thermal conductivity of ice (W/(m·K))
λ_{ins}	thermal conductivity of the insulation (W/(m·K))
λ_m	thermal conductivity of the mortar filling (W/(m·K))
λ_N	thermal conductivity of nitrogen (W/(m·K))
λ_p	thermal conductivity of pipe (W/(m·K))
λ_s	thermal conductivity of solid grains (W/(m·K))
λ_{SG}^{frozen}	thermal conductivity of frozen SG layer (W/(m·K))
λ_{Tb1a}^{frozen}	thermal conductivity of frozen Tb1a layer (W/(m·K))
$\lambda_{SG}^{unfrozen}$	thermal conductivity of unfrozen SG layer (W/(m·K))
$\lambda_{Tb1a}^{unfrozen}$	thermal conductivity of unfrozen Tb1a layer (W/(m·K))

λ_w	thermal conductivity of unfrozen water (W/(m·K))	ρ_i	density of ice (kg/m^3)
μ_N	dynamic viscosity of nitrogen (Pa·s)	ρ_N	density of nitrogen (kg/m^3)
ϕ	porosity	ρ_s	density of solid grains (kg/m^3)
φ'	friction angle (°)	ρ_w	density of water (kg/m^3)
		$(\rho c_p)_{eq}$	equivalent volumetric thermal capacity (J/(K·m^3))

(2008) provide a comprehensive overview of the practical and critical aspects of the AGF technique.

Monitoring should be implemented at all stages of AGF. Immediately after installation, the as-built positions of the freeze and secondary holes are generally checked by, e.g., inclinometers for vertical holes and three-axis magnetometers/accelerometers or fibre optic-based techniques for horizontal holes (Noureldin et al., 2000). Temperature sensors installed in secondary holes are used to measure the temperature of the ground at different positions around the freezing pipes. The frozen wall continuity and water tightness may be checked by controlled pumping and piezometric head measurements inside and outside the excavation area. Finally, the displacements of the ground around the surface and at depth during freezing and thawing are measured to evaluate and control potential adverse effects on existing structures. Among other reasons, insufficient monitoring or inadequate data reduction, leading to poor interpretation (Viggiani & Casini, 2015), have induced significant issues, often associated with over- or under-sizing of the frozen body, in extreme cases leading to flooding of the excavation (Czaja et al., 2020).

AGF is a highly coupled thermo-hydro-mechanical (THM) process (Nishimura et al., 2009; Alzoubi et al., 2020). The application of a cooling thermal load induces a heat transfer process and redistributes the temperatures in the soil according to the thermal properties of the constituent materials. It also modifies the groundwater flow, especially during ice formation, and induces mechanical deformation (Sopko, 2019; Zhao, 2019). The volumetric deformation is related not only to the expansion of water on freezing by about 9% of its volume but also to temperature-driven water migration, resulting in larger than initial water contents in the frozen body. During thawing, the excess water accumulated as ice must be expelled with transient excess pore water pressures and final contraction that may be larger than the initial expansion due to irreversible modifications to the soil structure (Chamberlain & Gow, 1979). Finally, high seepage velocities can pose significant challenges to the formation of a continuous frozen wall of the required thickness (Pimentel et al., 2012; Huang et al., 2018).

Various authors have used monitoring data collected from real case studies to develop numerical models to simulate different aspects of the process with various levels of complexity. Purely mechanical analyses (M) are regularly carried out to evaluate the stability of the excavation under the protection of the frozen wall. Often, the analyses are simply carried out by changing the mechanical properties of the design soil body affected by freezing (Russo et al., 2015). If the viscous nature of the frozen ground is modelled explicitly, a finite time to failure is predicted for relatively high load levels (Schindler et al., 2023, 2024). Afshani et al. (2015) have modelled the effects of freezing and thawing using a thermo-mechanical (TM) approach, in which the mechanical properties of the soil are linked to the computed temperature obtained by heat propagation analyses. Thermal analyses (T) are suitable for optimisation studies to define, e.g., the layout of the freezing pipes and the extension of the frozen body during AGF operation (Gioda et al., 1994; Levin et al., 2021; Sancho Calderon, 2022). As the thermal properties of the ground depend markedly on temperature, particularly across 0 °C, and it is necessary to include the latent heat release on phase change, the partial differential heat equation must be integrated numerically. Coupled thermo-hydraulic (TH) analyses are required if there is significant water seepage, and convective heat transport cannot be ignored. TH analyses

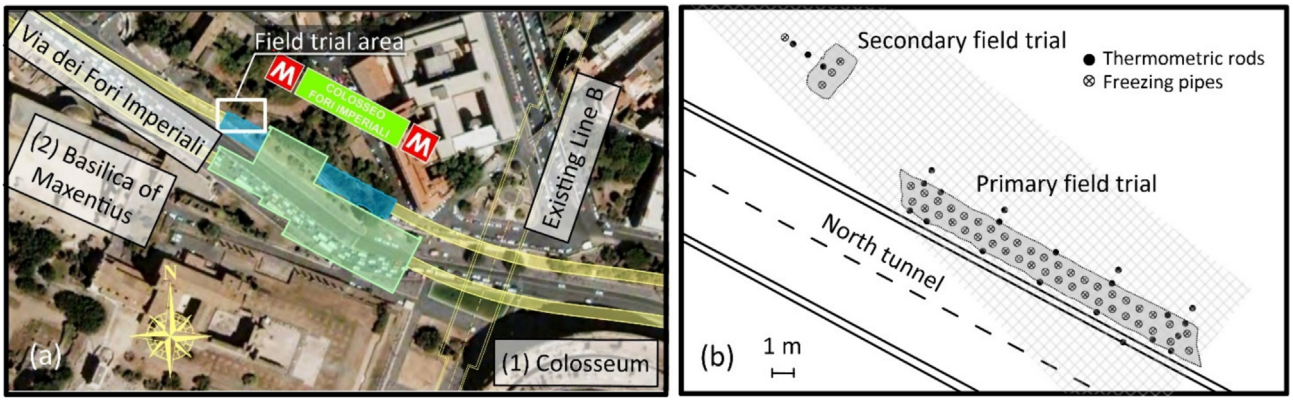

Fig. 1. (a) Plan view of the area of the Colosseo-Fori Imperiali station (https://metrocspa.it/stazione/fori-imperiali/), and (b) particular of the AGF field trial area.

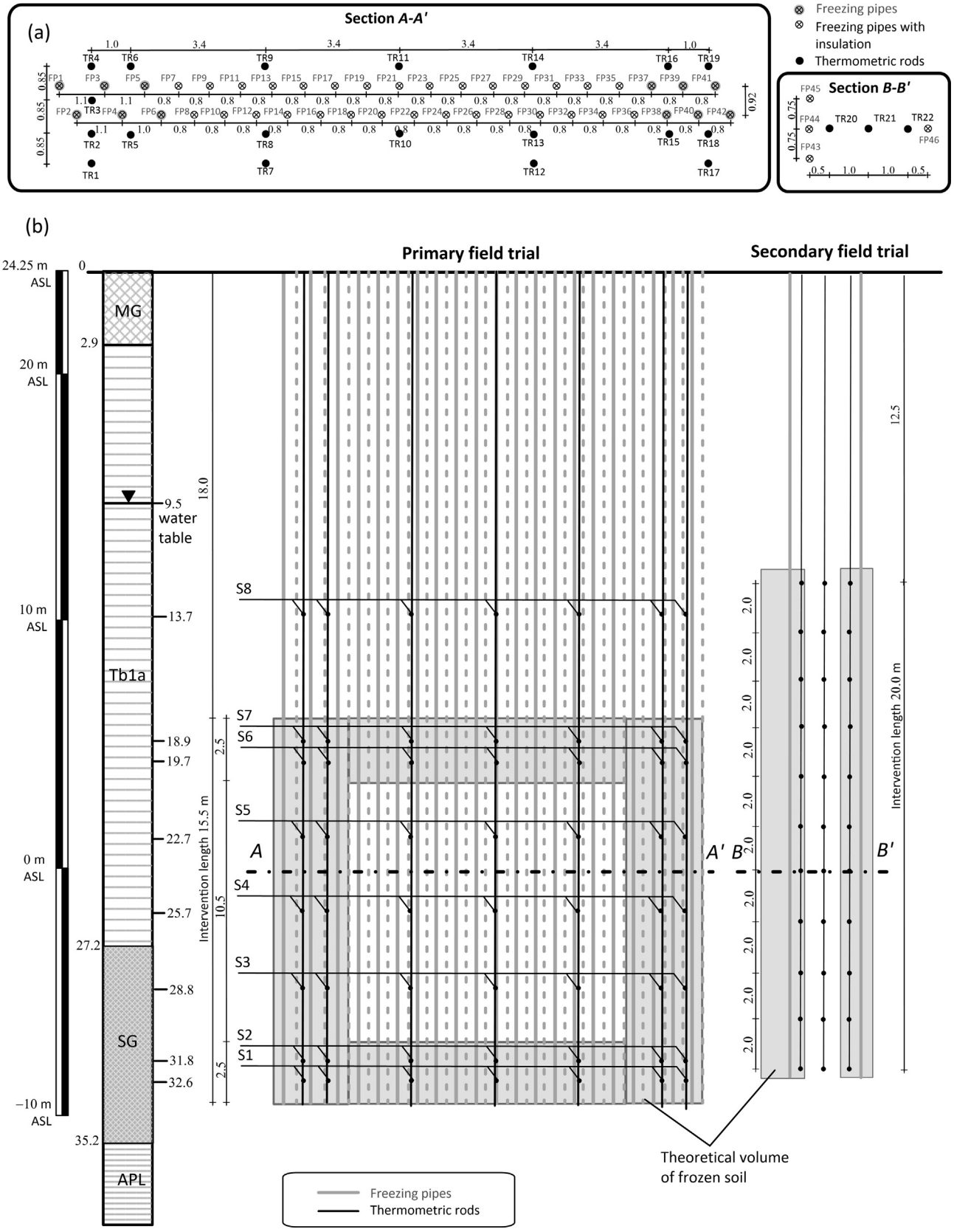

Fig. 2. (a) Plan, and (b) lateral configurations of the primary and secondary AGF field trials. (Unit: m).

require additional constitutive relationships governing the dependency of the unfrozen water content and permeability on temperature (Meschke et al., 2015; Li et al., 2020; Casini et al., 2023). Ground heave on freezing and subsequent settlement on thawing, particularly relevant in transition soils, can only be predicted by fully coupled THM analyses (Zhou et al., 2013; Viggiani & Casini, 2015; Zhelnin et al., 2022). However, THM analyses are still not widely used in practice due to the complex system of non-linear, time-dependent, coupled partial differential equations that must be solved and the often intricate layout of the freezing works that make the simulations computationally prohibitively intensive.

This work was motivated by the collection of extensive monitoring data from a field trial of AGF in central Rome. Their interpretation permitted to gain insight into the transient freezing process in stratified subsoils. The data also supported the development and validation of a three-dimensional thermo-hydraulic numerical model including an innovative procedure to define the thermal boundary conditions at the freezing pipes. In previous studies, these boundary conditions have often been simplified as a constant temperature, equal to a fraction of that of the circulating coolant. In this study, a simplified approach that solves the heat transfer problem between the coolant and the surrounding soil was developed to establish a physically grounded definition of the thermal boundary. Moreover, equivalent 2D models are examined to reduce complexity and computational demands, achieving results comparable to those of the 3D model.

2 Case study: Colosseo-Fori Imperiali Station

The preliminary design of the third line of Roma Underground, or Line C, was approved in October 2002 by the Municipality of Rome, and the tender for detailed design and construction was awarded in February 2006. Once completed, the line will cross the city centre from the northwest to the southeast, intersecting twice with the existing metro Line A and once with Line B, and reaching out to the eastern suburbs for a total length of about 26 km and 29 stations. To date, twenty-two stations and 19 km of line are operational. The construction of the stations included in the stretch of the line passing the historical centre is ongoing; Porta Metronia Station and Colosseo-Fori Imperiali Station are expected to open in 2025, and the works at Venezia Station have just started. All three stations mentioned above fall within an area of great archaeological, historical and artistic value and construction is facing significant challenges connected to the presence of archaeological remnants, the geotechnical characteristics of the soil, excavation below the water table, and the necessity of minimising the effects on the historical and monumental heritage.

Colosseo-Fori Imperiali Station plays a strategic role in the mobility plan supported by Line C; besides being in one of the most visited monumental areas in the world, it is a fundamental interchange with the existing Line B, as outlined in Fig. 1(a). The station has an irregular layout with a maximum length of 150 m and a maximum width of 34 m. It develops under the Via dei Fori Imperiali, close to the archaeological complex of the Colosseum (1) and Basilica of Maxentius (2). The station box was excavated top-down between diaphragm walls with a thickness of 1.20 m and a length of 48 m within the boundaries of the area left barren of archaeological remnants by the demolition of the Velia Hill in the 1930s (Perrone, 1955). Since the required length of the platforms for the trains of Line C is 110 m, and the maximum available length of the archaeological barren area on the north side of the station is limited, to create the platform tunnel, it was necessary to widen the north running tunnel by conventional mining on either side of the station box.

At the design stage, two alternative ground treatment methods were considered to ensure the safe completion of the tunnel enlargement works, namely chemical and cement injections, and AGF. In both cases, the design of the ground improvement works was based on the results of field trials. For the first method, which was the one eventually adopted for construction, the field trial was used to define the composition of the injection mixtures and various injection parameters. For AGF, the field trial was crucial to establish the response of the subsoil to the imposed freezing loads, verify nitrogen consumption, and check the volumetric response at the ground surface.

3 AGF field trials

As shown in Fig. 1(b), two field trials were carried out close to the north running tunnel, immediately above the station tunnel enlargement. The primary field trial included 42 freezing pipes (FP1 to FP42) and 19 thermometric rods (TR1 to TR19) to measure the temperature in the ground. The secondary field trial consisted of only four freezing

Table 1
Main physical and mechanical properties of the soil layers.

Soil layers	w (%)	γ (kN/m^3)	w_L (%)	I_P (%)	φ' (°)	c' (kPa)	s_u (kPa)	G_0 (MPa)
MG	–	17.0	–	–	34	–	75	–
Tb1a	27.0	19.3	25	15	31	20	110	209
SG	28.0	20.0	–	–	35	–	–	1371
APL	21.5	20.4	46	21.5	26	50	250	463

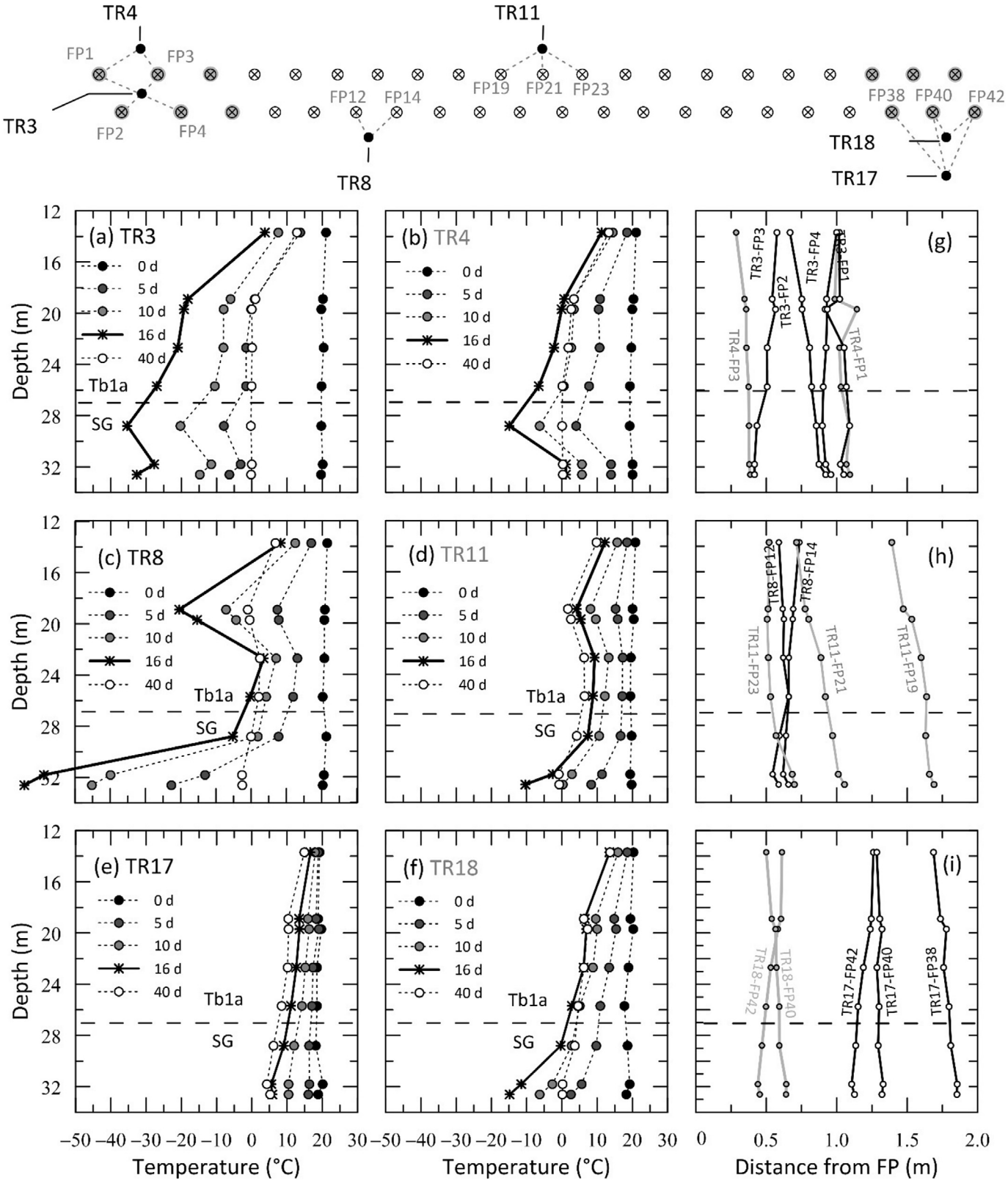

Fig. 3. (a)–(f) Profiles of recorded temperature at different times along six selected thermometric rods in the primary field trial, and (g)–(i) as-built distance between the six thermometric rods and the neighbouring freezing pipes, accounting for deviations from the design position of both freezing and monitoring holes.

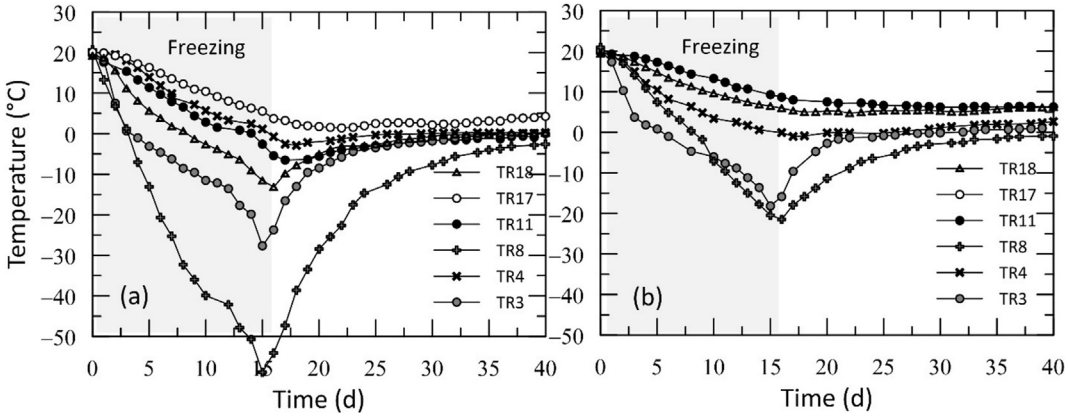

Fig. 4. Time evolution from selected thermometric rods of the primary field trial at depths of (a) 31.8 m (sensors S2) in the SG layer, and (b) 18.9 m (sensors S7) in the Tb1a layers, respectively.

pipes (FP43 to FP46) and three thermometric rods (TR20 to TR22). Figure 2 shows a plan and a lateral view of the field trial configurations. In the primary field trial, the 42 pipes were arranged in two rows, 0.92 m apart of 21 pipes each, installed vertically from the ground surface. The spacing between the freezing pipes of each row was 0.8 m, except for the last three freezing pipes on the left, which are spaced at 1.1 m. The secondary field trial consisted of three freezing pipes arranged in a row, with a spacing of 0.75 m, and a fourth pipe placed 3 m away along the transversal direction.

To simulate ground freezing around the tunnel perimeter in a hypothetical enlarged section of the station tunnel, the freezing pipes of the primary field trial were insulated along the portions that did not require freezing. Specifically, the freezing pipes along the abutments (FP1–FP6 and FP37–FP42) were activated only between 18 and 33.5 m below ground level (BGL) and thermally insulated elsewhere. Instead, the central freezing pipes (FP7–FP36) were activated along two depth intervals of only 2.5 m to form the crown and the invert, as shown in Fig. 2(b). The freezing pipes of the secondary field trial were activated only between depths of 12.5 and 32.5 m BGL for direct comparison with the primary field trial in a more straightforward configuration.

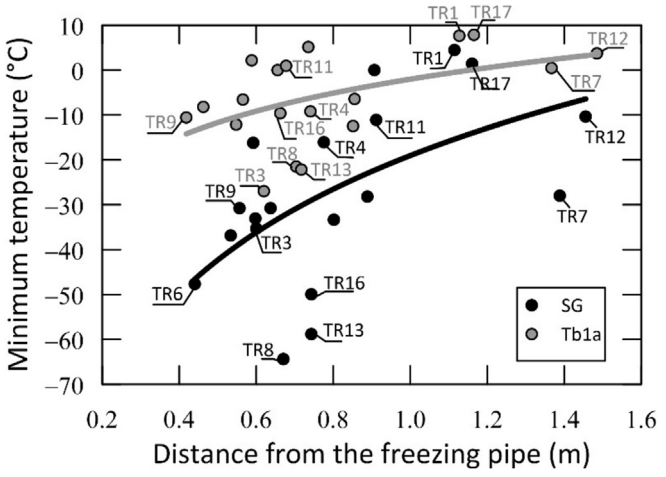

Fig. 5. Minimum temperature registered from the sensors of the primary field trial in the SG and Tb1a layers at all 21 thermometric rods as a function of the average as-built local distance between the thermometric rods and the two closest freezing pipes.

All the freezing pipes and the thermometric rods were assembled on-site and placed in the 34 m long perforation holes supported by steel casings with a diameter of 168 mm and a thickness of 10 mm. Before installing the freeze pipes and the thermometric rods, the as-built positions of the perforation holes were measured using inclinometers. The freezing pipes consisted of an external tube made of stainless steel with a diameter of 60 mm and a thickness of 3 mm, in 6 m long joined together by threaded and welded sleeves and an 18 mm diameter copper inner tube with a thickness of 1 mm. Along the non-active portion, a 25 mm thick cover made by an insulating elastomer protected by PVC provided the thermal insulation for the freezing pipes. The thermometric rods consisted of steel tubes with a diameter of 25 mm, in 6 m lengths joined using threaded sleeves. Eight temperature sensors (S1 to S8) were placed along each thermometric rod of the primary field trial between the depths of 32.6 and 13.7 m, for a total of 152 sensors. Eleven temperature sensors (S1 to S11) were placed for each thermometric rod of the secondary field trial between the depths of 32.0 and 22.0 m, with a regular spacing of 2.0 m, for a total of 33 sensors. Additional temperature sensors were installed in the nitrogen exhaust towers to monitor the discharge temperature, ranging between −75 and −130 °C.

Figure 2 also shows the soil profile at the location of the AGF field trials, as obtained from the boreholes carried out to install the freezing pipes and thermometric rods and perform cross-hole testing. Starting from the ground surface, the soil profile comprises a layer of made ground (MG), consisting of heterogeneous sands and silts, with a thickness of about 3 m, underlain by a layer of fine silty sand (Tb1a) including discontinuous clayey lenses, with significant vertical and horizontal variability and a

thickness of about 24 m, extending to a depth of about 27 m BGL. This is followed by an 8 m thick layer of sand with gravel (SG) and, from a depth of 35 m, a base deposit of stiff over consolidated silty clay (APL). These ground conditions are consistent with the general soil profile in Colosseo-Fori Imperiali Station, as defined by the extensive geotechnical investigations carried out between 1995 and 2011 (Viggiani et al., 2022; Metro C S.c.p.A., 2011a).

Pore water pressure measurements show that the hydraulic regime within the Tb1a layer is almost hydrostatic, with a piezometric head of 14.8 m above sea level (ASL); a slightly lower piezometric head of about 13.4 m ASL is observed in the SG layer (Metro C S.c.p.A., 2011b). The recorded regime of pore water pressure is compatible with downward seepage and head dissipation through the finer-grained lenses in the Tb1a layer. Viggiani et al. (2022) also observed a slight decrease in the piezometric head in the SG layer moving from the southeast to the northwest.

Table 1 summarizes the physical and mechanical properties of the soil layers, derived from extensive and repeated ground investigations (GIs) conducted since the preliminary design phase (1995). The physical properties of the soils were determined from both disturbed and undisturbed samples collected during successive GIs. The small-strain soil stiffness was evaluated from cross-hole tests. For the coarse-grained soils (MG and SG layers), the mechanical properties were estimated mainly from in situ test data, including standard penetration tests (SPTs) and cone penetration tests (CPTs). In contrast, the strength parameters for the finer-grained soils (Tb1a and APL layers) were derived from laboratory triaxial tests (Viggiani et al., 2022; Metro C S.c.p.A., 2011a).

4 Monitoring data

Trevi S.p.A carried out the field trial of AGF in July 2011. The set-up included an open-circuit nitrogen distribution system fed by two silos, with capacities of 30 and 5 m^3. During activation, liquid nitrogen circulated at an average flow rate of 3.5 m^3/h for 16 days. The total liquid nitrogen consumption during activation was about 1.28×10^3 m^3 (or 80 m^3/d).

Figrue 3(a)–(f) shows the profiles of the recorded temperature at different times along six thermometric rods in the primary field trial, namely TR3 and TR4 near the left frozen abutment, TR8 and TR11 in the central area, and TR17 and TR18 near the right frozen abutment. Figure 3 (g)–(i) shows the as-built distance between the six thermometric rods and the neighbouring freezing pipes, which can be larger or smaller than the design value due to deviations from the design position of both freezing and monitoring holes.

In most cases, the temperatures attained their lowest values on the last freezing day ($t = 16$ d). The temperature recorded by thermometric rods placed at a more considerable distance from the freezing pipes, such as, e.g., TR11 and TR17, was rarely below 0 °C and, due to thermal inertia, continued to decrease monotonically even after the end of freezing ($t > 16$ d). At all times, the temperature profiles

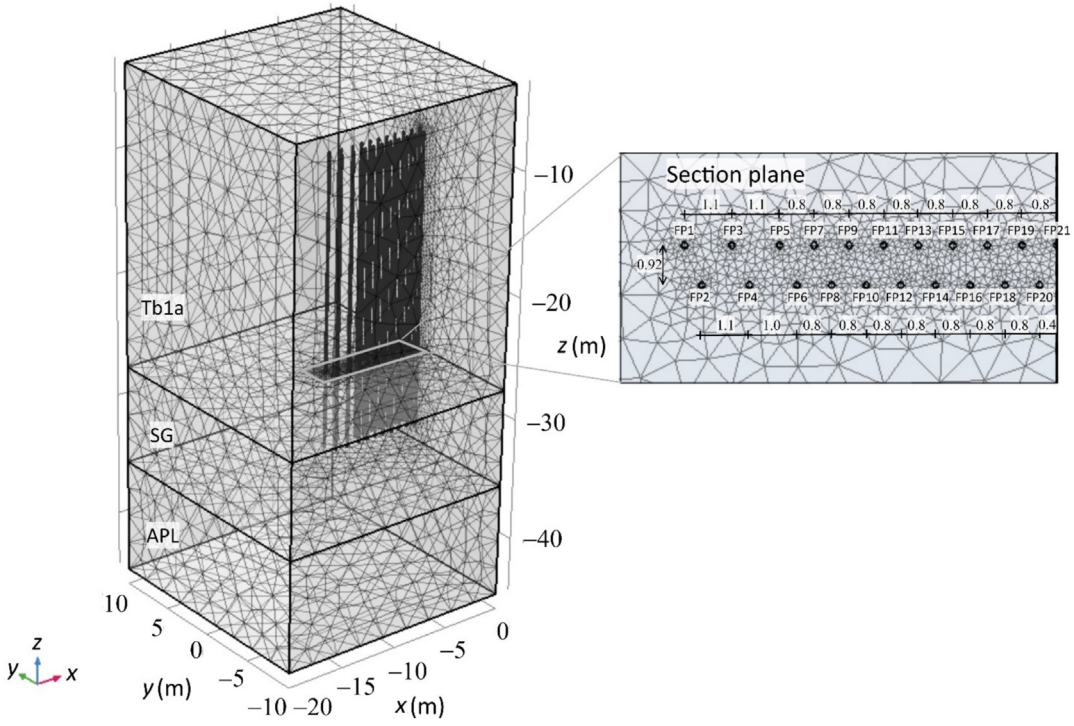

Fig. 6. Three-dimensional model of the primary field trial created in the Comsol Multiphysics® environment with details of the positions of the freezing pipes and mesh refinement. (Unit: m).

Table 2
Physical, hydraulic and thermal properties of the layers adopted in the numerical analyses.

Soil layers	Physical properties		Hydraulic properties				Thermal properties	
	ρ_s	ϕ	k_{sat}	m	P	S_{res}	λ_s	$c_{p,s}$
	(kg/m^3)		(m/s)		(kPa)		(W/m·K)	(J/kg·K)
Tb1a	2626	0.41	5×10^{-6}	0.42	35	0.08	2	800
SG	2844	0.44	1×10^{-4}	0.4	4	0	5	600
APL	2674	0.36	1×10^{-7}	0.39	180	0.15	1.5	1000

from thermometric rods TR8 and TR11, located in the central area, showed two minima at depths of 19 and 33 m, corresponding to the crown and the invert of the frozen wall. The thermal insulation of the freezing pipes appears not to be perfect, as indicated by decreasing temperatures over time at sensors S3, S4, S5 (22–29 m depth), and S8 (13.7 m depth).

The soil type significantly affected heat transmission, with temperatures in the SG layer consistently lower than those in the finer-grained Tb1a layer at all thermometric rods; at the end of freezing, the minimum temperature recorded at TR8 in the SG layer was below −50 °C and around −20 °C in the Tb1a layer. This is due to heat transmission in coarse-grained soils being faster than in fine-grained soils due to the higher thermal conductivity of the solid particles (Chang and Lacy, 2008), but also to the fact that the coolant at the base of the freezing pipe is inherently colder as its flow along the outer annulus is directed upwards.

The larger spacing of the freezing pipes on the left of the field trial does not significantly affect the temperature profiles, e.g., thermometric rods TR4 (left) and TR18 (right). The smaller the distance between the freezing pipe and the thermometric rod, the lower the recorded temperature. For instance, the temperatures recorded at TR17 were consistently higher than those at TR18 because its average distance from the freezing pipes is more than double that of TR18.

Another influencing factor is the number of neighbouring freezing pipes; for instance, the temperatures recorded at TR3, which had four neighbouring freezing pipes (FP1, FP2, FP3 and FP4), were consistently lower than the temperatures at TR4, which had only two neighbouring freezing pipes (FP1 and FP3).

Figure 4 illustrates the time evolution from selected thermometric rods of the primary field trial at depths of 31.8 m (sensors S2) and 18.9 m (sensors S7) in the SG and the Tb1a layers, respectively. As expected, all temperatures decreased during freezing, with a higher rate for smaller distances between the thermometric rod and the active freezing pipe. In the SG layer (Fig. 4(a)), at the end of freezing, the temperature of the sensors in the rods closer to the freezing pipes (TR3, TR8, TR18) increased rapidly, tending to an asymptotic temperature of about 0 °C after 24 days. The sensors in the rods placed further away from the freezing pipes (TR4, TR11) show the effects of thermal inertia, with a minimum value reached after the end of freezing. The trends of the recorded temperatures in the Tb1a layer (Fig. 4(b)) are very similar. In contrast, the minimum temperatures achieved at the end of freezing are higher, and the response of the sensor in thermometric rod TR18 appears dampened.

Figure 5 shows the minimum temperature measured in the SG and Tb1a layers at all 21 thermometric rods as a function of the average as-built local distance between the thermometric rod and the two closest freezing pipes. The data scatter observed can be attributed to multiple sources: the spatial heterogeneity of the natural soil deposits, which significantly impacts the transient thermal response of the soil, the mutual distances between the freezing pipes and the measurement points, and the temperature of the coolant at the outlet which varies between −75 and −130 °C. However, the logarithmic trend lines in Fig. 5 illustrate the relationship between the minimum temperature and the distance from the freezing pipes, clearly indicating consistently lower temperature values measured in the SG layer.

5 Numerical simulations

The TH-coupled model used to simulate AGF integrates the water mass and thermal energy balance equations, providing the temperature and water pressure field distribution throughout the domain during the freezing process. This model neglects volume changes induced by the freezing (assuming a constant porosity $\phi = \text{const}$). This assumption is realistic for coarse-grained soils, such as the SG layer, which are not susceptible to frost heave (Armstrong & Csathy, 1963), but it may be less appropriate for finer-grained soils like the Tb1a layer. In situ monitoring of displacement, however, revealed limited effects of the freezing operation at the soil surface, with recorded frost heave values less than 5 mm. Moreover, the focus of this study is on the thermo-hydraulic aspects of frozen wall formation, so that the mechanical effects associated with soil surface displacement were deliberately neglected. Appendix A reports the complete derivation of the governing equations and describes all the constitutive relations.

In the case study under examination, a three-dimensional model is required to account for the layout of the freezing pipes properly, the soil stratigraphy, the hydraulic regime, and the overall formation of the frozen

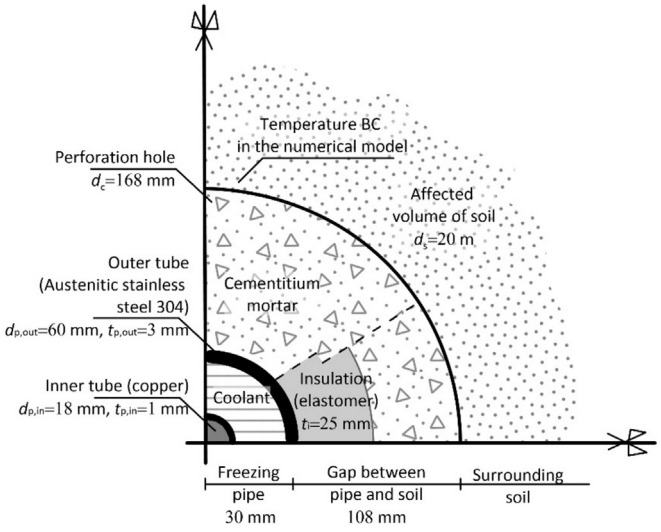

Fig. 7. Transversal section of the freezing pipe showing the layers filling the gap between the outer tube of the freezing pipe and the surrounding soil. All shown diameters are external.

wall. However, a fully TH-coupled three-dimensional model is computationally costly, and in the following, the monitored data were interpreted using a de-coupled formulation. A stationary pore water pressure regime was imposed throughout the integration domain, and only the thermal energy balance equation was integrated into time and space. This is reasonable because there is no background seepage, and AGF operations affected only marginally the initial distribution of pore water pressures.

Figure 6 reports the three-dimensional model of the primary field trial created in the Comsol Multiphysics® (Comsol, 2023) environment and introduces the space coordinate system. The domain is a block with a width of 20.0 m, a depth of 20.0 m, and a height of 41.5 m, reproducing half of the primary trial on the side containing the wider-spaced abutment freeze pipes. The layer of made ground is not included in the model because it is poorly characterised, its thickness (2.9 m) is relatively small, and its presence does not affect the study results. The mesh consists of 323 104 elements, 27 416 boundary elements, 10 948 edge elements and 514 vertex elements, with automatic refinement near the freezing pipes to enhance simulation accuracy. Along the pipe boundary, the mesh uses "mapped" elements with an "extremely fine" size, calibrated for "general physics" with a maximum element size of 0.887 m and a minimum size of 0.009 m. For the rest of the domain, "free tetrahedral" elements with a "normal" element size are used (max. 4.44 m, min. 0.79 m), similarly calibrated for "general physics".

The vertical plane corresponding to $x = 0$ is assumed to be a thermal and hydraulic symmetry plane. All the other sides of the domain are far enough from the freezing pipes not to be affected by AGF operations. Therefore, a constant undisturbed temperature $T_0 = 19.5$ °C is imposed on those sides; from the hydraulic point of view, piezometric heads of 14.8 m ASL and 13.4 m ASL were imposed in the Tb1a and SG layers, respectively, and a fictitious impervious boundary was introduced to separate the two layers and maintain the two hydraulic heads.

Table 2 summarises the physical, thermal and hydraulic properties of the layers adopted in the numerical analyses. The physical properties are consistent with those reported in Table 1. In situ Lefranc tests were used to measure the saturated hydraulic conductivity (Metro C S.c.p.A., 2011a). The van Genuchten (1980) retention model parameters, P, m, and S_{res}, for layers Tb1a and APL, were estimated from the grain size distributions using the empirical method by Arya and Paris (1981). The water retention curve parameters of the coarser layer, SG, were chosen to be in the typical ranges for coarse soils (Wilson, 1990), since its grading is outside the range of application of Arya and Paris (1981). The thermal properties of solid grains were set to obtain equivalent thermal conductivities and volumetric heat capacities that would agree with literature values for similar soils (Frivik, 1981; Pahud, 2002). The equivalent thermal conductivity is defined as a geometric mean of the thermal conductivities of the different phases weighed by volumetric fractions according to Gens (2010):

$$\lambda_{eq} = \lambda_s^{(1-\phi)} \lambda_w^{S_w\phi} \lambda_i^{S_i\phi}, \quad (1)$$

where S_i and S_w are the ice and liquid water degrees of saturation defined as the volume of ice or water, respectively, over the volume of voids; λ_s is the thermal conductivity of the solid particles; $\lambda_w = 0.6$ W/(m·K) and $\lambda_i = 2.22$ W/(m·K) are the thermal conductivities of the liquid water and ice phases, respectively.

The equivalent volumetric thermal capacity is defined as a linear combination of the volumetric thermal capacities of the different phases, weighed by their volume fractions:

$$(\rho c_p)_{eq} = c_{p,s}\rho_s(1-\phi) + c_{p,w}\rho_w S_w \phi + c_{p,i}\rho_i S_i \phi, \quad (2)$$

where ρ_s, $\rho_w = 1000\,kg/m^3$, and $\rho_i = 916.2\,kg/m^3$, and $c_{p,s}$, $c_{p,w}$= 4.18 kJ/(kg·K), and $c_{p,i}$ = 2.05 kJ/(kg·K) are the densities and the mass thermal capacities of solid particles, water, and ice, respectively.

AGF was modelled by imposing an assigned temperature T_p, at the boundary of the freezing pipes. Heat transfer from the soil to the pipes decreases the temperature in the soil, driving the phase change of the pore water into ice. Only the portions of the freezing pipes below the groundwater table were considered. The pipes were modelled as cylindrical impervious boundaries with a diameter of 0.168 m, corresponding to the size of the external steel casing that supported the perforation holes.

6 Thermal boundary conditions at freezing pipes

The temperatures at the boundary of the pipes T_p, were computed from a simplified steady-state heat transfer analysis, considering heat convection between the coolant and

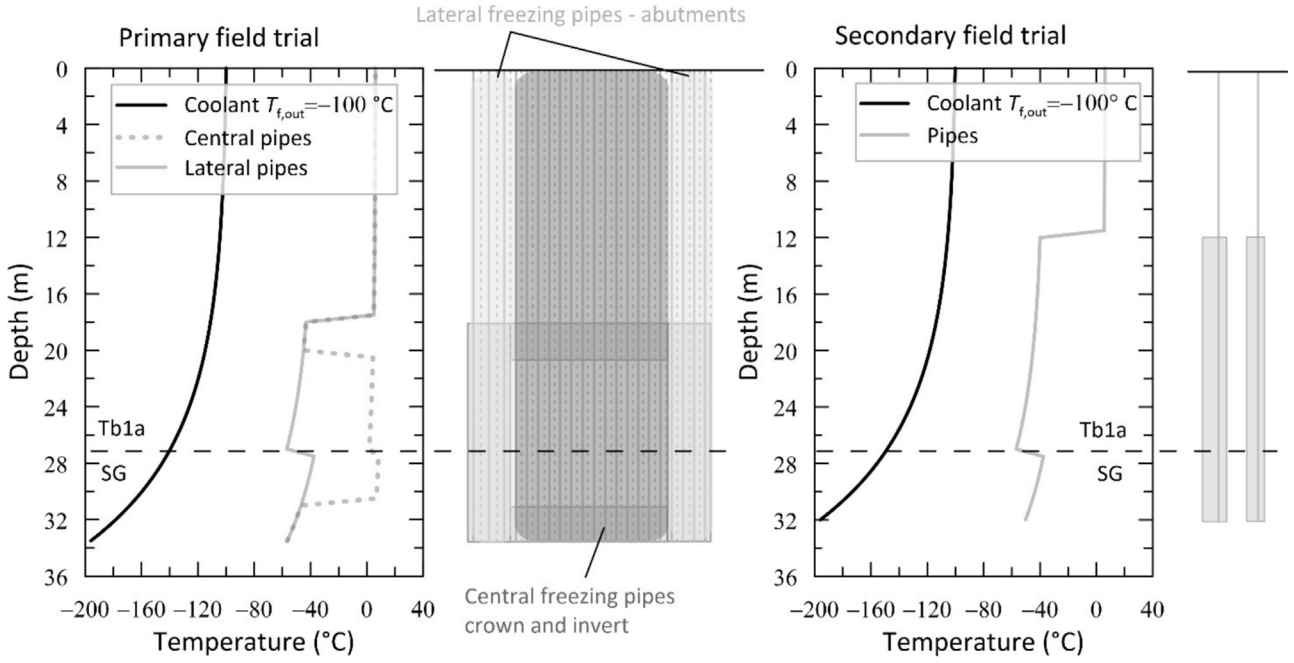

Fig. 8. Steady-state temperature profiles of the coolant and freezing pipe boundary conditions for the primary and secondary field trials.

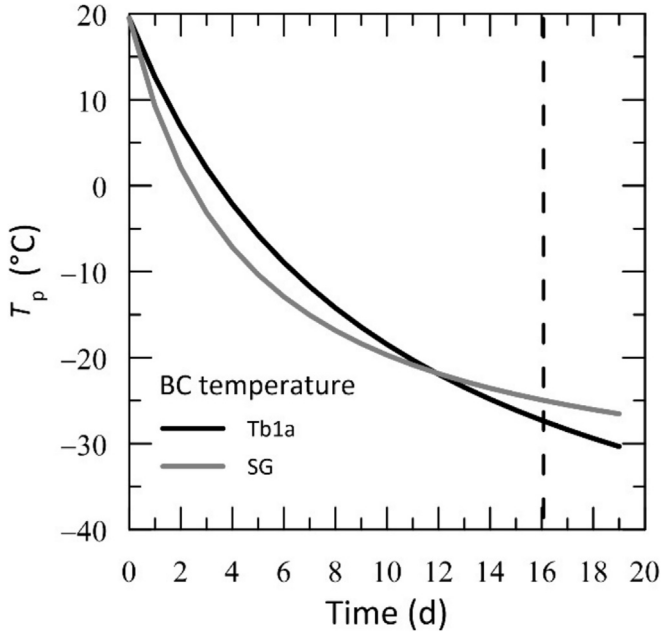

Fig. 9. Time evolution of the temperature boundary conditions at the freezing pipes at $z = 27.2$ m following a hyperbolic decreasing trend according to Eq. (6).

the walls of the pipe and the radial heat conduction through the different solid layers separating the coolant from the soil.

Liquid nitrogen is stored at a temperature of −196 °C. During circulation, it absorbs heat from the surrounding environment, increasing its temperature, and undergoes a phase change. It is eventually released in the atmosphere in its gas phase at a measured discharge temperature that varies between −75 and −130 °C. Nitrogen discharge temperature varies from pipe to pipe due to factors such as location of phase change, thermal dispersion, and differences in insulation along the pipes. This study simplifies the heat exchange problem by decoupling (i) the forced heat convection of the coolant along the pipe from (ii) the radial heat conduction extending to the surrounding soil.

In the analyses, a single tube with an equivalent diameter with respect to the outer annulus was considered, in which the coolant flows upward, exchanging heat with the surrounding environment through convection. In this simplified model, the cooling effect from the descending flow within the inner tube is disregarded; however, the cooling loss associated with the ascending flow is enhanced. The evolution of the coolant temperature along the freezing pipe due to forced heat convection was computed equating the heat absorbed by the coolant and the heat flux exchanged by convection with the outer surface of the pipe and integrating along the pipe length, L_p. The steady-state evolution of the fluid temperature along the length coordinate of the pipe $T_f(x_p)$ can therefore be obtained as follow, see Appendix B for details:

$$T_f(x_p) = T_s - (T_s - T_{f,in}) \exp\left(-\frac{h_N \pi d_{p,eq} x_p}{\dot{m}_N c_{p,N}}\right), \quad (3)$$

where T_s is the surface temperature of the outer tube, $T_{f,in}$= −196 °C is the inlet temperature at the bottom end of the freezing pipe, $h_N = 30.67$ W/(m^2•K) is the nitrogen convection heat transfer coefficient, $\dot{m}_N = 0.017$ kg/s is the nitrogen mass flow rate, $c_{p,N} = 1050$ J/(kg•K) is the nitrogen specific heat capacity, and $d_{p,eq} = 0.036$ m is the internal

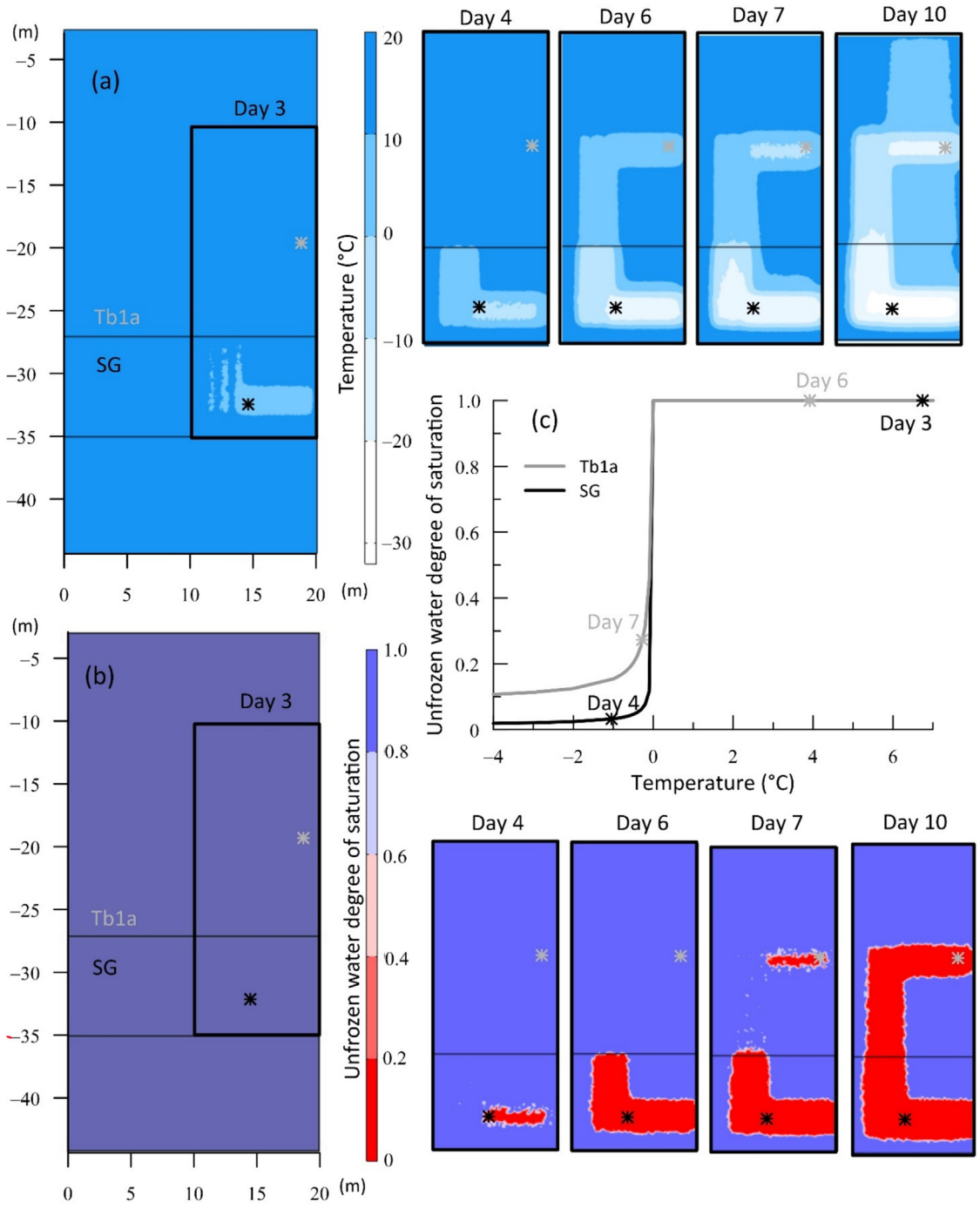

Fig. 10. Predicted contours of (a) temperature and (b) unfrozen water degree of saturation for the primary field trial at different times on the vertical plane ($y = 0$) between the two rows of freezing pipes, and (c) ice characteristic curves for Tb1a and SG layers together with the points representing the thermo-hydraulic state at the two locations indicated in the contour plots at different times.

diameter of the outer pipe. Calculations were based on a liquid nitrogen discharge of 3.5 m^3/h in 46 freezing pipes disposed parallelly for 16 days corresponding to the AGF activation phase. The temperature T_s can be obtained from Eq. (3) by setting the temperature of the fluid at $x_p = L_p$ equal to the average discharge temperature among all freezing pipes, $T_f = -100$ °C, which yields to $T_s = -98.9$ °C. As the coolant is not directly in contact with the surrounding soil, radial heat dispersion must be considered. Figure 7 shows the layers filling the gap between the outer tube of the freezing pipe and the surrounding soil. The thermal boundary condition in the numerical model of the field trials is the temperature at the interface with the ground, located ~50 mm away from the external tube of the freezing pipes. A layer of high-conductivity cementitious mortar fills the gap between the

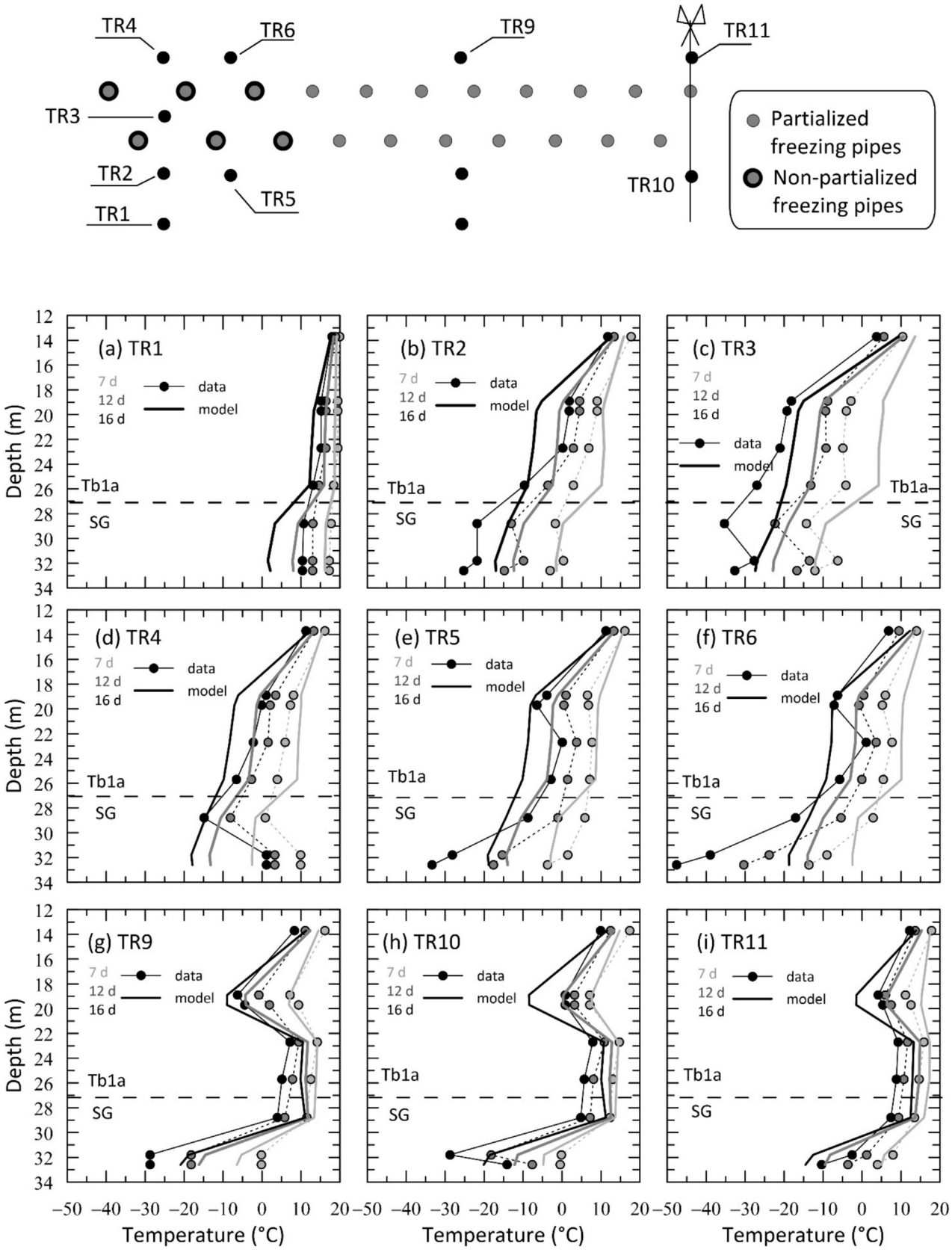

Fig. 11. Temperature profiles with depth obtained from numerical simulations compared with the monitored data from the primary field trial.

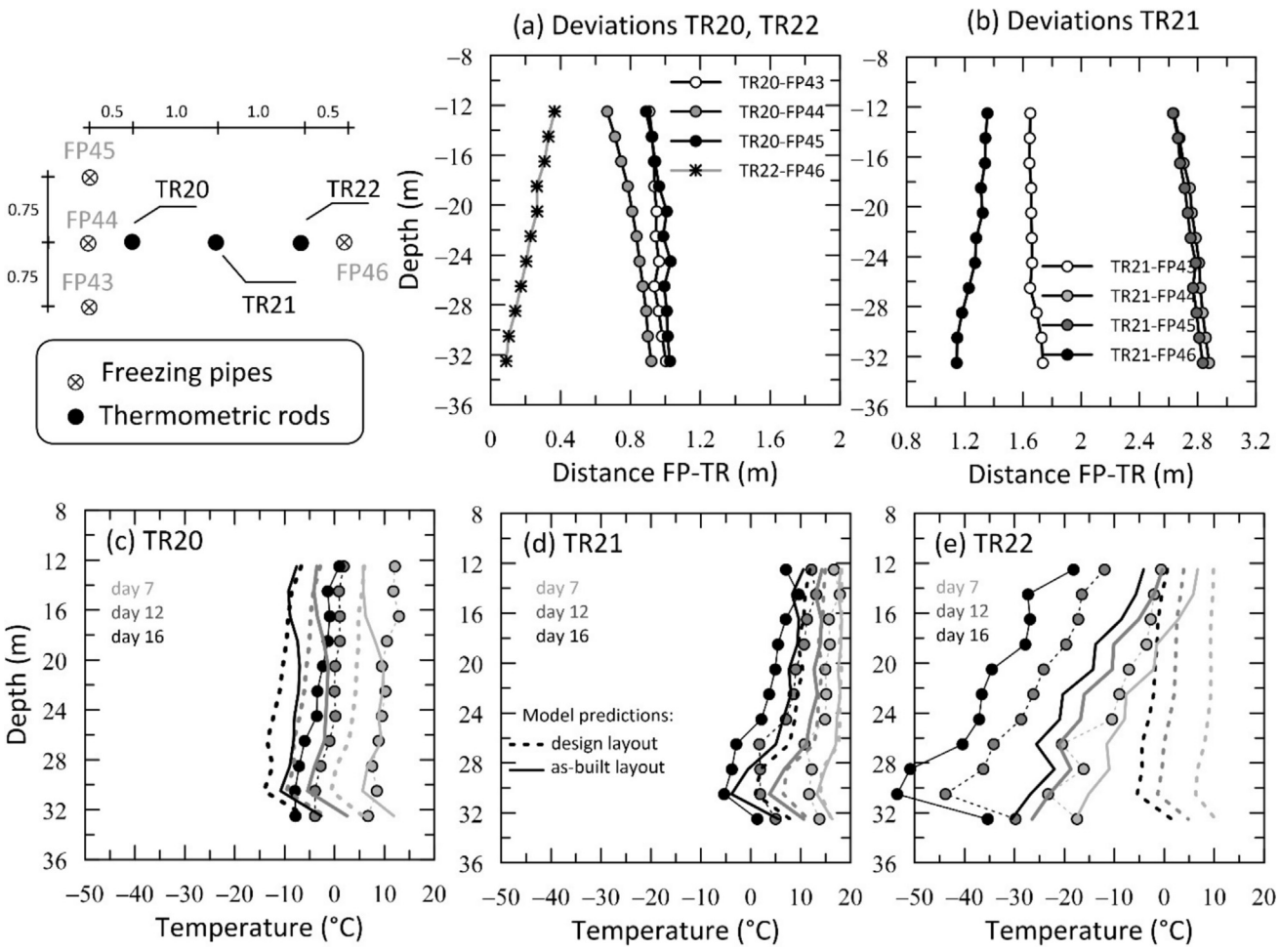

Fig. 12. Numerical predictions of the secondary field trial both for the design (dashed lines) and as-built (continuous lines) layout, compared with the observed temperatures.

freezing pipe (diameter $d_{p,out} = 60$ mm, thickness $t_{p,out} = 3$ mm) and the soil, as shown in Fig. 7. Along the insulated portions, the pipe is surrounded by an insulated elastomer with a thickness $t_i = 25$ mm.

To characterise the radial heat transfer of an elongated, slender circular heat exchanger such as a freezing pipe, the thermal power, $\dot{Q}$, conventionally expressed per metre length of the thermally active portion can be expressed by (Laloui & Rotta Loria, 2019):

$$\dot{Q} = \frac{\Delta T}{\sum_i R_i} = \frac{\Delta T}{R_{1,\text{fluid}} + R_{2,\text{pipe}}(+R_{3,\text{insul}}) + R_{4,\text{mortar}} + R_{5,\text{soil}}}, \quad (4)$$

where R_i is the time-independent thermal resistance, and ΔT is the temperature variation. The thermal resistance associated with the heat transfer process depends on the geometry of the pipes and the surrounding layers. Specifically, it accounts for the thermal resistance due to the fluid thermal convection ($R_{1,\text{fluid}}$), thermal conduction through the outer pipe thickness ($R_{2,\text{pipe}}$), insulation when present ($R_{3,\text{insul}}$), cementitious mortar ($R_{4,\text{mortar}}$), and the affected volume of soil ($R_{5,\text{soil}}$). Consistently with the assumptions made on the boundary condition of the numerical model of the field trial, this has been taken to extend 10 m from the axis of the freezing pipe. The steady state position of the frozen front separating the frozen and unfrozen region of the soil, with different thermal resistances, was obtained iteratively. Appendix B details the calculations of the thermal resistances, and the properties considered for each layer.

Once the thermal power $\dot{Q}$ per unit length is known, the variation of temperature at the boundary with the soil can be evaluated as

$$\Delta T_{\text{coolant-soil}} = \dot{Q}\left[R_{1,\text{fluid}} + R_{2,\text{pipe}}(+R_{3,\text{insul}}) + R_{4,\text{mortar}}\right]. \quad (5)$$

Figure 8 reports the steady-state temperature profile of the coolant and freezing pipe boundary conditions for the primary and secondary field trials. Different soil types affect heat dispersion by conduction: higher thermal conductivity values, such as in the SG layer, result in more significant heat losses. Along the insulated portions of the pipes, the computed average steady-state temperatures were $T_p^{\infty} = 4$ °C and 7 °C, in the Tb1a and SG layers, respectively. In the active portion of the pipes, the

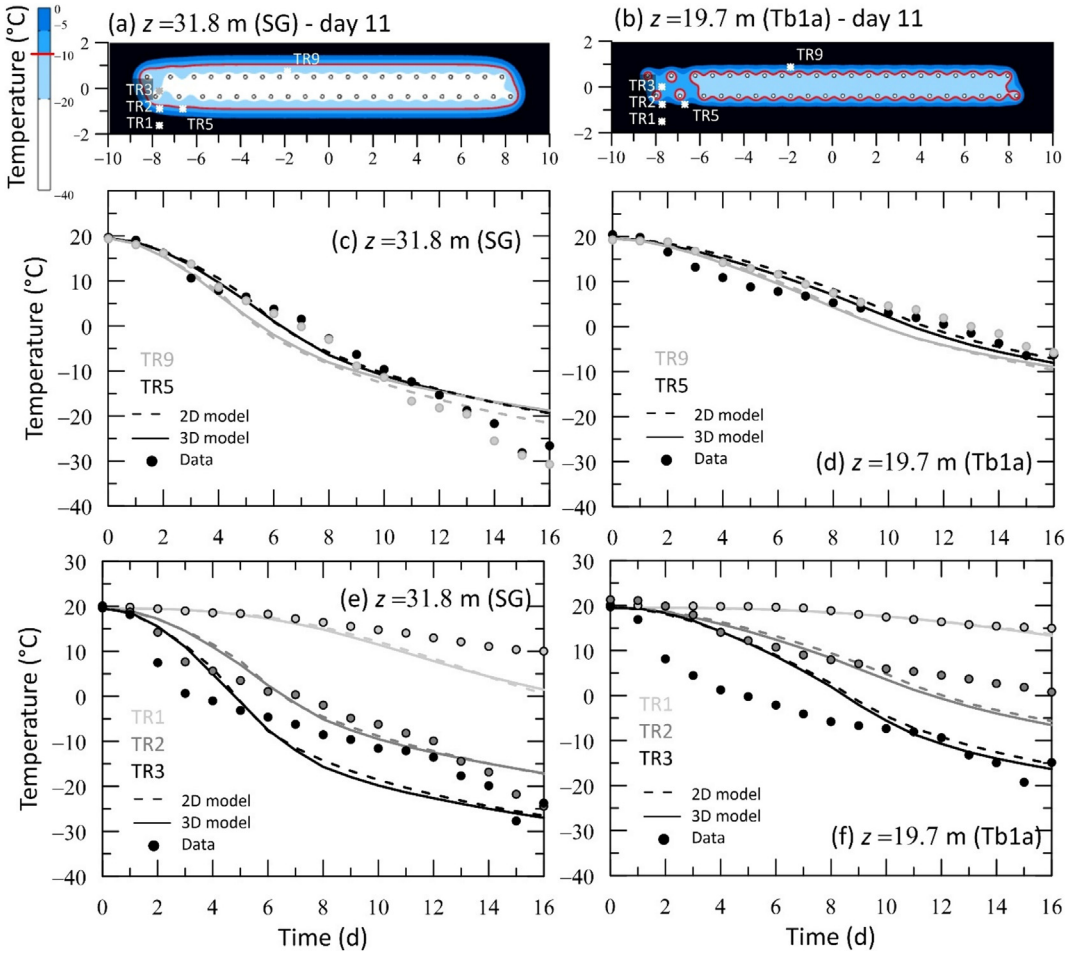

Fig. 13. Results from simplified 2D models of the primary field trial at depths 31.8 m (SG layer) and 19.7 m (Tb1a layer). (a)–(b) Contours of temperature after 11 days from AGF activation, (c)–(f) time histories of temperatures obtained in (c)–(d) thermometric rods TR5, TR9, and (e)–(f) TR1, TR2 and TR3 at depths 31.8 m (S2) and 19.7 m (S6).

steady-state temperatures decrease with depth according to the temperature profile of the coolant, ranging from $T_p^{\infty} = -57$ °C to −43 °C in the SG layer and from $T_p^{\infty} = -57$ °C to −37 °C in the Tb1a layer. Finally, it was assumed that the steady state temperature at the pipe boundaries would only be achieved asymptotically in time following a hyperbolic law:

$$T_p = T_0 - \frac{t}{\frac{t}{|T_p^{\infty} - T_0|} + M}, \tag{6}$$

where $T_0 = 19.5$ °C is the soil undisturbed temperature. This means that at the end of the 16 days of freezing, the temperature at the boundary of the freezing pipes has not yet reached the steady state value (see Fig. 9). In Eq. (6), $1/M$ represents the initial slope of the temperature variation with time and depends on the material (Vitel et al., 2015), with steeper initial temperature variations with time for coarser-grained materials. Here, we assumed values of M of 0.13 d/K and 0.08 d/K for the Tb1a and SG layers, respectively. The ratio between the values of M for the two materials is taken to be equal to the ratio between their thermal diffusivities, defined as the thermal conductivity over the specific heat capacity.

7 Model prediction

Figure 10 illustrates the predicted contours of (a) temperature and (b) unfrozen water degree of saturation for the primary field trial at 4, 5, 7, 8, and 10 days after activation of freezing on the vertical plane ($y = 0$) between the two rows of freezing pipes. According to the evidence from the monitored temperatures (Figs. 3 and 4), the frozen soil body forms first in the SG layer. This is because of the higher thermal conductivity of the SG layer, and because the coolant, flowing upwards, has lower temperatures at the tip of the freezing pipes. Temperatures below 0 °C are reached around day 4 and day 7 in the SG and Tb1a layers, respectively. By day 10, a continuous frozen wall appears to be fully formed. Due to the larger spacing between freezing pipes, the temperature decrease is less uniform along the abutments than at the invert and the crown. Figure 10(c) shows the ice characteristic curves for the Tb1a and SG layers and the points representing the

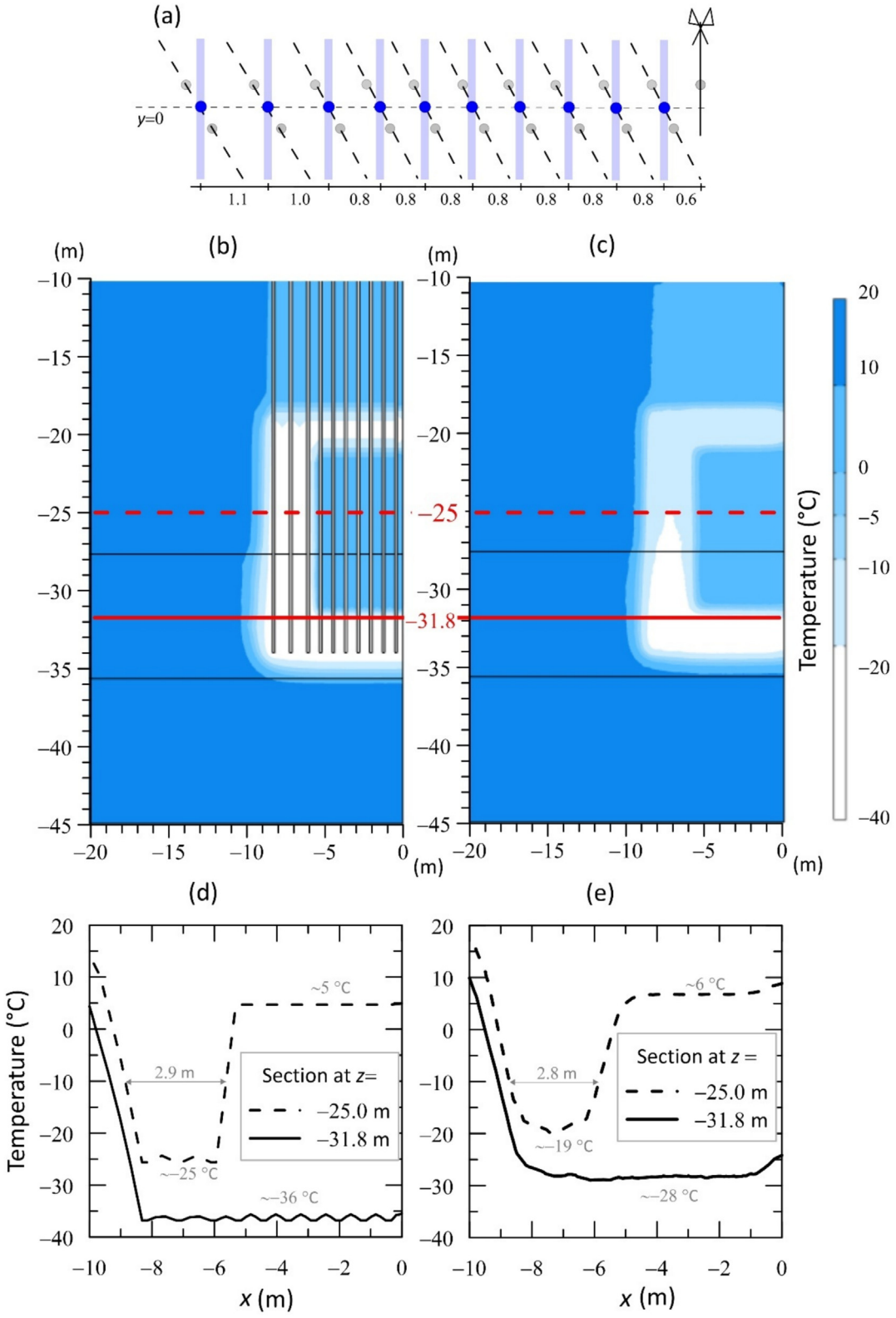

Fig. 14. Results of the 2D simplified model of the primary field trial, corresponding to the vertical plane at $y = 0$, where (a) "virtual" freezing trenches were modelled, (b)–(c) contours of temperatures after 16 days from activation from the 2D and entire 3D models, and (d)–(e) profiles of temperature along sections at depths 25 m (Tb1a) and 31.8 m (SG), respectively.

thermo-hydraulic state at the two locations indicated in the contour plots at different times. The progressive development of the frozen soil body occurs over a narrow range of temperatures below 0 °C; the unfrozen water content of the soil decreases rather abruptly from $S_w = 1$ to the residual value, $S_{res} = 0.08$ and 0.01 for the Tb1a and SG

layers, respectively. Although often the design specification of the frozen wall thickness is given in terms of relatively low target temperatures, from the hydraulic point of view, as shown by the plots in Fig. 10, an impervious wall is obtained as soon as the residual unfrozen degree of saturation is achieved (Casini et al., 2023).

Figuer 11 compares the observed temperature profiles along selected thermometric rods from TR1 to TR6 and from TR9 to TR11 with the numerical predictions after 7, 12, and 16 days from the beginning of freezing. The numerical predictions are in good qualitative agreement with the monitoring data, reproducing well the faster freezing in the SG layer and the impact of the distance of the measurement point from the freezing pipe.

The numerical predictions at the depth of the shallowest sensors indicate a decrease in temperature over time because the analyses account for the imperfect thermal insulation of the non-active portions of the freezing pipes. This also applies to the non-active segments between the depths of 22 and 28 m along thermometric rods TR7, TR8 and TR9.

The numerical predictions for the primary field trial were carried out using its design layout, which can differ from the as-built layout due to unavoidable deviations from the vertical of both freezing and observation holes. This can be responsible for at least some observed discrepancies between the measured and predicted temperatures. Indeed, while the numerical predictions for thermometric

Table 3
Range of parameters adopted in the parametric analyses.

Parameter	Symbol	Values	Baseline value
Thermal conductivity of solid grains	λ_s (W/m· K)	1.25, 2.5, 5	5
Specific heat capacity of solid grains	$c_{p,s}$ (J/kg·K)	600, 1200, 2400	600
Ice entry pressure	P (kPa)	4, 40, 400	4
Hydraulic conductivity	k_{sat} (m/s)	1×10^{-4}, 1×10^{-6}, 1×10^{-8}	1.0×10^{-4}

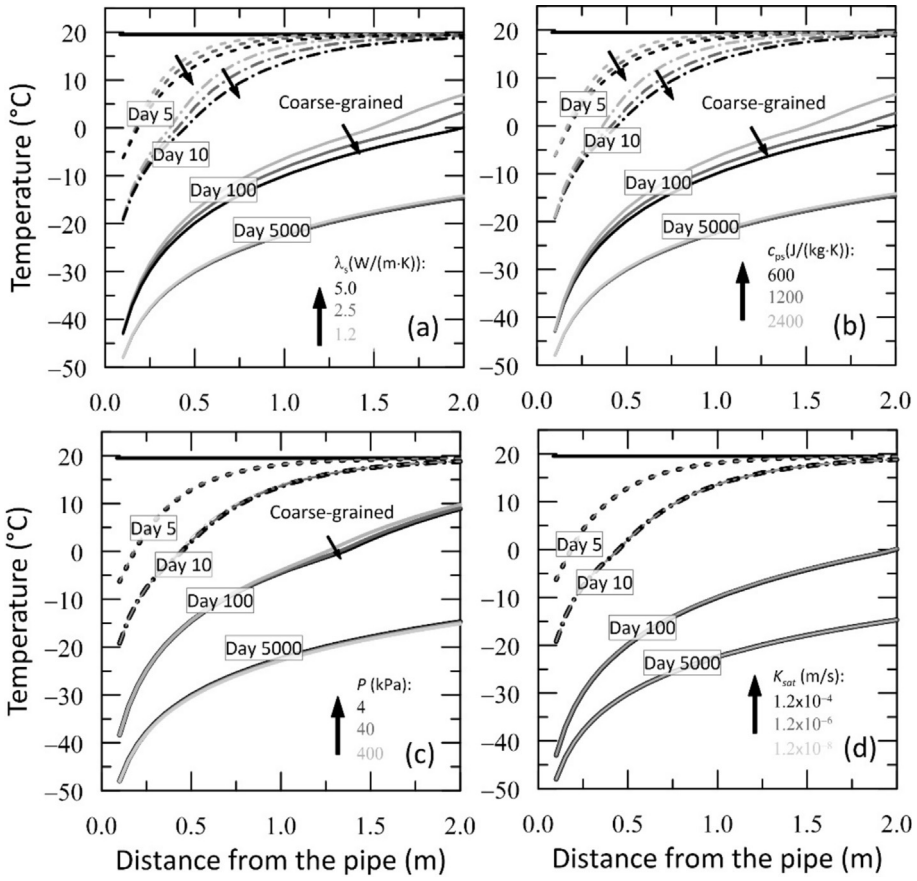

Fig. 15. Profile of temperature at various times along the radial distance from the freezing pipes varying thermal (thermal conductivity λ_s and specific heat capacity of solid grains $c_{p,s}$) and hydraulic properties (ice entry pressure P, and hydraulic conductivity k_{sat}).

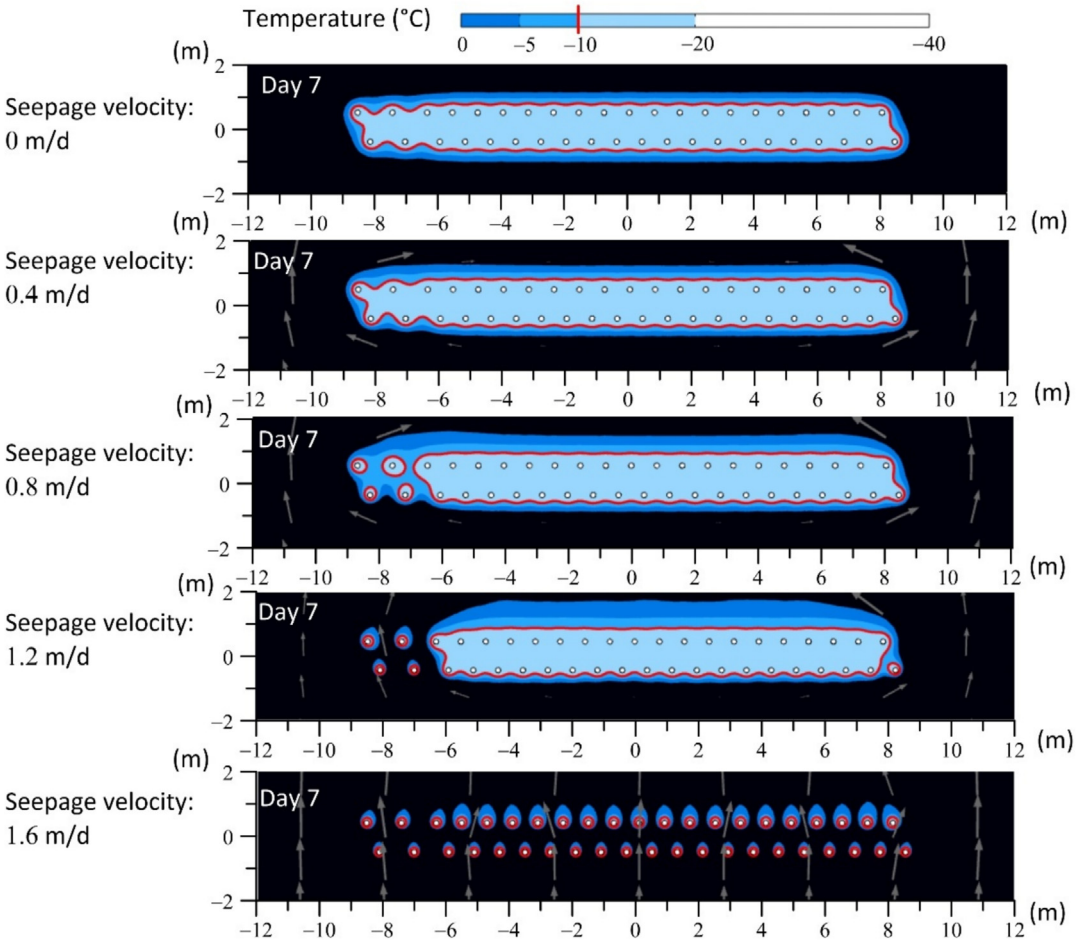

Fig. 16. Contours of temperature obtained from simplified 2D plane models of the primary field trial at SG layer depths after 7 days from AGF activation varying the seepage velocity from 0 to 1.6 m/d.

rods placed at the same nominal distance from the freezing pipes, such as TR2 and TR4 or TR5 and TR6, are similar to one other, the corresponding monitored data often differ.

As a validation exercise, the observations in the secondary field trial were predicted using the same numerical procedures and parameters adopted for the primary field trial. Because, in this case, the deviations of the freezing pipes and of the observation holes from the intended design positions were significant, see Fig. 12(a) and (b), the analyses were repeated both for the design (dashed lines) and the as-built (continuous lines) layouts. The numerical model incorporated freezing pipe deviations through rigid motions based on linear interpolation of the measured deviations in space, while sensor deviations were directly applied to individual measuring points. Modelling deviations had minimal impact on the predicted temperatures for TR21, see Fig. 12(d), which align well with the observed values for the design and as-built layouts. If deviations are not considered, the temperatures predicted along TR20 are lower than observed due to a more considerable as-built distance between the freezing and observation holes. Accounting for deviations along TR22 is crucial to capture the correct temperature profile with depth because of the significant reduction in the distance between TR22 and FP46.

8 Simplified approaches

For practical applications, it may be desirable to adopt numerical models with simplified two-dimensional layouts to reduce computational effort. For instance, if the length of parallel freezing pipes is significantly larger than the characteristic size of a constant excavation section, a two-dimensional domain perpendicular to the freezing pipes can be adopted. This corresponds to assuming plane strain conditions and no water or heat flow in the direction perpendicular to the integration domain. On the other hand, a fully three-dimensional analysis may be needed when freezing pipes are not parallel, the intervention extension is limited (e.g., inclined passageways and cross passages), or there are three-dimensional features in the soil stratigraphy and/or the hydraulic regime.

This section explores and compares the results obtained from simplified two-dimensional plane models of the primary field trial with those obtained from the entire three-dimensional model described above.

Figure 13(a) and (b) shows the contours of temperature at depths of 31.8 and 19.7 m in the SG and the Tb1a layer, respectively, after 11 days from activation obtained using 2D models with the same temperature boundary conditions as those described in Section 5. The different thermal properties of the two layers significantly impact the formation of the frozen wall, conventionally defined as the volume of soil at a temperature below −10 °C and indicated in the figure as a red line. This is 2 m thick at the invert (Fig. 13(a)) in the SG layer and less than 1 m at the crown (Fig. 13(b)) in the Tb1a layer. In both cases, the increased spacing at the abutment has a negative effect on the thickness of the frozen wall, which, after 11 days, is still not continuous in the Tb1a layer. Figure 13 also shows the time histories of the temperatures obtained in thermometric rods TR5 and TR9, Fig. 13(c) and (d), and TR1, TR2, and TR3, Fig. 13(e) and (f), at depths 31.8 m (S2) and 19.7 m (S6). The predictions from the 2D and 3D models are very close to one another, with maximum differences of less than 5 °C at any time, and to the experimental data. This indicates that three-dimensional effects play a negligible role in the prediction of the temperature fields in the AGF field trial at Fori Imperiali.

Figure 14 shows another possible 2D model of the primary field trial, corresponding to the vertical plane at $y = 0$ between the two rows of freezing pipes. Although this section does not intersect any pipe, "virtual" freezing trenches were placed at a position barycentric between the two actual rows of pipes, see Fig. 14(a). Once again, the temperature boundary conditions at the freezing trenches are the same as those described in Section 5. The contours of temperature obtained after 16 days from activation from the 2D and 3D models are qualitatively comparable; see Fig. 14(b) and (c). For a more detailed, quantitative comparison between the results from the two models, Fig. 14(d) and (e) shows the profile of temperature along two sections of the contours at depths of 25 m, through the abutment in the Tb1a layer, and of 31.8 m, through the invert in the SG layer, respectively. The temperatures predicted by the 2D model within the frozen body are lower than those predicted by the 3D model and obviously equal to the thermal boundary condition at 16 days, where the section intersects a "virtual" freezing trench. On the other hand, the predicted extension of the frozen wall is remarkably similar between the two analyses. This is because, as indicated by existing results (Viggiani & Casini, 2015), the temperatures obtained at the middle point of a line of freezing pipes are not substantially different from those at the middle point of only two pipes.

9 Sensitivity analyses

Parametric analyses were conducted to investigate the influence of thermal and hydraulic properties and background seepage velocities on the evolution of the freezing process.

The activation of a single freezing pipe of a length of 20 m, fully embedded in a uniform subsoil, was modelled in axis-symmetric conditions. A steady state temperature of $T_p^{\infty} = -50$ °C was applied at the pipe boundary; once again, this was reached asymptotically in time according to Eq. (6) with $M = 0.1$ d/K. The domain is 20 m high, and its radius is large enough (20 m) for its temperature not to be affected by the freezing pipe at 5000 days. The baseline subsoil properties and hydraulic regime were set to be those of the SG layer. The effect of the variation of four parameters, namely the thermal conductivity λ_s, the specific heat capacity $c_{p,s}$ of the solid particles, the ice entry pressure value P, and the saturated hydraulic conductivity k_{sat}, was examined. In each set of analyses, one parameter was varied while the others were kept constant and equal to their baseline values. Table 3 summarises the ranges of parameters adopted in the analyses.

Figure 15 shows the profiles of temperature at various times (day 5, 10, 100, and 5000) with distance from the freezing pipe; arrows indicate the direction in which the curves would shift for coarser-grained materials. In the short term, the key parameters affecting the temperature profiles are the thermal conductivity and the specific heat capacity of solid grains, see Fig. 15(a) and (b). Coarse-grained soils with higher thermal conductivities and lower specific heat capacities exhibit faster heat transfer; however, the thermal properties do not affect the long-term (day 5000) temperature distribution. These analyses indicate that the formation of a frozen wall of specified thickness may lag by several days based on the thermal properties of the soils; therefore, in AGF applications, nitrogen activation may have to last longer in finer-grained materials. Because there is no background seepage, both hydraulic parameters, namely the ice entry pressure value P, and the saturated hydraulic conductivity k_{sat}, have a negligible impact on the heat transfer process, see Fig. 15 (c) and (d).

A sensitivity analysis on the effect of seepage velocity was further conducted using the 2D plane model from the primary field trial. The domain geometry was the same as in Fig. 13(a), corresponding to a horizontal section at the SG layer. The thermal boundary conditions were identical to those explained in Section 5, while the hydraulic boundary conditions were configured to impose a horizontal water seepage flow from the bottom to the top of the domain, perpendicular to the rows of freezing pipes. The range of seepage velocities investigated spanned from 0 to 1.6 m/d. Figure 16 reports a comparison of temperature contours evaluated after 7 days of freezing activation for different water seepage regimes. An imposed seepage velocity of 0.8 m/d delayed the formation of a continuous frozen wall by several days with respect to the no background seepage condition, where a continuous frozen wall at a temperature lower than −10 °C fully developed by day 7. This occurs on the left abutment, characterised by a larger spacing between the freezing pipes. At an even higher

seepage velocity, e.g., 1.6 m/d, none of the frozen soil cylinders developing around the freezing pipes merged into another after 7 days of activation. This result agrees with the recommendation about the critical seepage velocity, 1–2 m/d, reported in the literature (Andersland & Landanyi, 2003).

10 Conclusions

This paper presents a detailed analysis of the extensive monitoring data from a field trial of AGF, conducted in connection with the construction of Colosseo-Fori Imperiali Station of Line C of Roma Underground.

A coupled TH three-dimensional finite element model was developed to back-analyse the field results, whose hydraulic and thermal parameters were calibrated based on the results of the geotechnical site investigation, literature data, and empirical methods. Special attention was given to the definition of appropriate thermal boundary conditions at the freezing pipes. These were computed from a simplified steady-state heat transfer analysis, considering heat convection between the coolant and the walls of the pipe and the radial heat conduction through the different solid layers separating the coolant from the soil. The steady-state temperatures at the pipe boundaries are only achieved asymptotically in time.

Because the fully TH-coupled three-dimensional model of the field trials was computationally costly, and useless in the case of no background seepage, the back analysis of the monitored temperatures was carried out using a decoupled formulation. Deviations from the intended positions of both freezing pipes and thermometric rods played a relevant role, as shown by the results obtained for the secondary field trial, where these deviations were significant. For practical applications, it may be desirable to adopt numerical models with simplified two-dimensional layouts to reduce computational effort. This study confirmed that reasonable results are obtained from two-dimensional models as long as proper choices are made on the equivalent 2D layouts.

Sensitivity analyses were conducted to investigate the role of the thermal and hydraulic properties, as well as the water seepage regime, in the freezing process. In the absence of background seepage flow, the hydraulic properties had only a negligible effect on the predicted temperature distribution. Instead, the soil thermal properties significantly impact the transient temperature distributions, while not affecting the predicted long-term steady-state temperatures. Water seepage velocities greater than 0.4 m/d, flowing perpendicularly to the freezing pipes, strongly affect the shape and the continuity of the frozen wall, particularly in areas where the spacing between the freezing pipes is wider. For AGF applications, the formation of a frozen wall of specified thickness may require significantly more time in finer-grained materials than in coarser-grained materials or in coarse-grained materials under a significant seepage regime.

Data availability

The data that support the findings of this study are available from the corresponding author upon reasonable request.

CRediT authorship contribution statement

Giulia Guida: Writing – review & editing, Writing – original draft, Visualization, Validation, Software, Methodology, Formal analysis, Conceptualization. **Arianna Pucci:** Software. **Eliano Romani:** Resources, Investigation. **Giulia M.B. Viggiani:** Writing – review & editing, Methodology. **Francesca Casini:** Project administration, Conceptualization.

Declaration of competing interest

Giulia M.B. Viggiani is an Editorial Board Member for *Underground Space* and was not involved in the editorial review or the decision to publish this article. All authors declare that there are no competing interests.

Acknowledgement

We would like to acknowledge the Regione Lazio, which supported Dr. Giulia Guida's fixed-term position through POR-FSE 2014/20 – Contributions for the permanence of excellence in the academic world (No. 65629/2020). Ministry of Economic Development supported Dr. Arianna Pucci through the Frozen GeoLab – Proof of Concept project (G.U.n. 283 03/12/2019). Metro C S.c.p.A. provided access to the data. The Master dissertations of Roberta Angelucci and Luca Schillaci were the starting point of this study.

Appendix A Thermo-hydraulic model-governing equations

Hydraulic component

In a fully saturated soil undergoing freezing, pores between the grains are filled by water in either unfrozen or frozen phase ($S_i + S_w = 1$, where S_i and S_w are the ice and unfrozen water degrees of saturation defined as the volume of ice or water, respectively, over the volume of voids) (Guida et al., 2023).

According to the compositional approach (Bear & Cheng, 2010), the water mass balance is expressed in chemical species, thus accounting for both unfrozen water and ice. The change in water mass (liquid and ice) over time is equal to the net inflow/outflow, solely due to liquid water seepage:

$$\phi \frac{\partial}{\partial t}(\rho_w S_w + \rho_i S_i) = -\nabla \cdot (\rho_w \boldsymbol{u}), \tag{A1}$$

where ϕ is the porosity of the medium, $\rho_w = 1000\,\mathrm{kg/m^3}$ and $\rho_i = 920\,\mathrm{kg/m^3}$ are the unfrozen water density and

the ice density, and $\boldsymbol{u}$ is the velocity of the unfrozen water, defined according to the Darcy's law:

$$\boldsymbol{u} = -\boldsymbol{K}\nabla\left(\frac{p_w}{\rho_w g} + z\right), \tag{A2}$$

where p_w is the unfrozen water pressure, z is the vertical coordinate, and $\boldsymbol{K} = \boldsymbol{k}_{sat}k_{rel}$ is the unfrozen hydraulic conductivity tensor defined as the product of the saturated hydraulic conductivity tensor $\boldsymbol{k}_{sat}$ and the relative permeability function k_{rel}. According to the unsaturated soil framework, the relative permeability assumes values ranging between 0 and 1, proportionally to the unfrozen water degree of saturation (van Genuchten, 1980).

Assuming the water and the ice as incompressible $\left(\frac{\partial \rho_w}{\partial t} = \frac{\partial \rho_i}{\partial t} = 0\right)$, the first storage term in Eq. (A1) becomes

$$\phi\left(\rho_w \frac{\partial S_w}{\partial t} + \rho_i \frac{\partial S_i}{\partial t}\right) = -\nabla \cdot \left[-\frac{\boldsymbol{K}}{g}(\nabla p_w + \rho_w g)\right]. \tag{A3}$$

The unfrozen water degree of saturation S_w depends on suction s by the water retention curve reported in Eq. (A4) (van Genuchten, 1980). Under freezing conditions, suction s is defined as the difference between the pressure of the ice p_i and the pressure of liquid water p_w.

$$S_w = 1 - S_i = S_{res} + (1 - S_{res})\left(1 + \left(\frac{s}{P}\right)^{\frac{1}{1-m}}\right)^{-m}, \tag{A4}$$

where S_{res} is the residual unfrozen degree of saturation, and P and m are model parameters that depend on the soil and fluid type.

The thermo-hydraulic coupling is defined by the ice pressure, expressed as a function of the liquid water pressure p_w and the temperature T using the Clausius Clapeyron equation (Nishimura et al., 2009):

$$p_i = \frac{\rho_i}{\rho_w} p_w - \rho_i L \ln\frac{T}{273.15}, \tag{A5}$$

where $L = 334.72$ kJ/kg is the water latent heat of fusion. The degree of saturation of unfrozen water and ice depends on water pressure p_w and temperature T through suction. Applying the chain rule, the partial derivatives of Eq. (A3) can be rearranged as

$$\frac{\partial S_w}{\partial t} = -\frac{\partial S_i}{\partial t} = \frac{\partial S_w}{\partial s}\frac{\partial s}{\partial t} = \frac{\partial S_w}{\partial s}\left(\frac{\partial s}{\partial p_w}\frac{\partial p_w}{\partial t} + \frac{\partial s}{\partial T}\frac{\partial T}{\partial t}\right). \tag{A6}$$

The quantity "water capacity" C_w was introduced to define the partial derivative of the unfrozen water degree of saturation over suction, according to Bear and Cheng (2010):

$$C_w = -\phi\frac{\partial S_w}{\partial s} = \phi(1 - S_{res})\frac{m}{P(m-1)}\left(\frac{s}{P}\right)^{\frac{m}{1-m}}\left(1 + \left(\frac{s}{P}\right)^{\frac{1}{1-m}}\right)^{-m-1}. \tag{A7}$$

Developing the partial derivatives of Eq. (A6) and substituting them into Eq. (A3), the governing equation can be expressed as a function of the two unknowns, p_w and T:

$$\rho_w S\frac{\partial p_w}{\partial t} + (\rho_w - \rho_i)C_w\rho_i\frac{L}{T}\frac{\partial T}{\partial t} = -\nabla \cdot \left[-\frac{\boldsymbol{K}}{g}(\nabla p_w + \rho_w g)\right], \tag{A8}$$

where $S = \frac{(\rho_w - \rho_i)^2}{\rho_w{}^2}C_w$ is the storage term depending on the water capacity C_w.

Thermal component

The thermal energy balance equation is written assuming that the internal energy for the entire phases of the porous medium is the sum of the internal energies of each one of the three phases (Gens, 2010): solid (s), liquid (w) and ice (i). To ensure energy conservation, the change in internal energy must be equal to the net inflow/outflow of heat:

$$\frac{\partial}{\partial t}[E_s\rho_s(1-\phi) + E_w\rho_w S_w\phi + E_i\rho_i S_i\phi] = -\nabla \cdot (\boldsymbol{i}_c + \boldsymbol{j}_{Ew}), \tag{A9}$$

where $E_s = c_{p,s}T$, $E_w = c_{p,w}T$ and $E_i = -L + c_{p,i}T$ are the internal energies of the three phases weighted by the volume fractions; $c_{p,s}$ (see Table 2), $c_{p,w} = 4186$ J/(kg·K) and $c_{p,i} = 2100$ J/(kg·K) are the specific heat capacities of solid grains, liquid water and ice, respectively; $\boldsymbol{i}_c = -\lambda_{eq}\nabla T$ is the conductive flux defined according to the Fourier's law; λ_{eq} is the equivalent thermal conductivity, defined as a combination of the thermal conductivities of the different phases according to $\lambda_{eq} = \lambda_s^{1-\phi}\lambda_w^{S_w\phi}\lambda_i^{S_i\phi}$ where λ_s is the thermal conductivity of the solid particles (see Table 2), $\lambda_w = 0.6$ W/(m·K) and $\lambda_i = 2.14$ W/(m·K) are the thermal conductivities of the liquid water and ice phase, respectively; $\boldsymbol{j}_{Ew} = E_w\rho_w\boldsymbol{u}$ is the convective flux for the liquid water phase only, assuming the other steady.

Substituting the previous definitions, Eq. (A9) becomes

$$\frac{\partial}{\partial t}\left[c_{p,s}\rho_s(1-\phi)T + c_{p,w}\rho_w S_w\phi T + \left(-\frac{L}{T} + c_{p,i}\right)\rho_i S_i\phi T\right] = -\nabla \cdot \left[-\lambda_{eq}\nabla T + c_{p,w}T\rho_w\boldsymbol{u}\right]. \tag{A10}$$

Assuming that the variation in time and space of the degree of saturation is negligible in terms of thermal energy conservation compared to that of the temperature $\left(\frac{\partial S_w}{\partial t} = 0;\ \nabla \cdot (c_{p,w}T\rho_w\boldsymbol{u}) = c_w\rho_w\boldsymbol{u} \cdot \nabla T\right)$ and developing the partial derivatives, Eq. (A10) can be finally rewritten as

$$\frac{\partial}{\partial t}\left[c_{p,s}\rho_s(1-\phi)T + c_{p,w}\rho_w S_w\phi T + \left(-\frac{L}{T} + c_{p,i}\right)\rho_i S_i\phi T\right] = -\nabla \cdot \left(-\lambda_{eq}\nabla T\right) - c_{p,w}\rho_w\boldsymbol{u} \cdot \nabla T. \tag{A11}$$

Appendix B Heat propagation from the coolant to the soil

The nitrogen temperature rises from its controlled storage level of –196 °C in the tanks, to a measured discharge

value of about –100 °C. During circulation, it undergoes a phase change, absorbing heat from the surroundings and increasing its temperature. This study simplifies the heat exchange problem by decoupling (i) the heat convection of the fluid flowing upward in a single tube with an equivalent diameter with respect to the outer annulus of the freezing pipes from (ii) the radial heat conduction towards the surrounding soil. The effect of the descending flow within the inner tube is disregarded.

Heat-forced convection of the freezing coolant

The evolution of the coolant temperature along the length of the pipe is attributed to the heat absorbed dQ by the fluid during the ascending forced convection process, regulated by Newton's law of cooling:

$$\mathrm{d}Q = h_{\mathrm{N}}\left[T_{\mathrm{s}} - T_{\mathrm{f}}\left(x_{\mathrm{p}}\right)\right]\pi d_{\mathrm{p,eq}}\mathrm{d}x_{\mathrm{p}}\,, \tag{B1}$$

where h_{N} is the convection heat transfer coefficient for nitrogen, T_{s} is the temperature of the outer tube, T_{f} is the temperature of the circulating fluid, x_{p} is the length coordinate of the pipe and $d_{\mathrm{p,eq}}$ is the equivalent diameter of the outer annulus of the two co-axial tubes. The convection heat transfer coefficient (h_{N}) depends on the thermophysical properties and the state of the fluid. For fluids with Prandtl number Pr, ranging between 0.5 and 100 in turbulent regime, h_{N} can be evaluated according to the semi-empirical relation proposed by Colburn (1964):

$$h_{\mathrm{N}} = 0.023 c_{p,\mathrm{N}}\rho_{\mathrm{N}}V_{\mathrm{N}}\,\mathrm{Pr}^{-2/3}\mathrm{Re}^{-0.2}, \tag{B2}$$

where $c_{p,\mathrm{N}}$ is the specific heat capacity, ρ_{N} is the density, V_{N} is the velocity, and Re is the Reynolds number of the gas nitrogen. The fluid velocity was estimated based on the overall discharge rate of nitrogen, assumed to be evenly distributed across the 46 freezing pipes of the primary and secondary field trials. At −196 °C, nitrogen remains in its liquid state; however, during heat exchange in the outer annulus of the freezing pipes, liquid nitrogen transitions to the gas phase. Given a flow rate of $\dot{m}_{\mathrm{N}} = 0.017$ kg/s, the corresponding velocity of the gaseous nitrogen in the outer annulus is calculated as follow:

$$V_{\mathrm{N}} = \frac{\dot{m}_{\mathrm{N}}}{\rho_{\mathrm{N}}A_{\mathrm{ann}}} = 3.51\,\mathrm{m/s}. \tag{B3}$$

The Prandtl and Reynolds numbers evaluated for gas nitrogen are:

$$\mathrm{Re} = \frac{\rho_{\mathrm{N}}V_{\mathrm{N}}d_{\mathrm{p,eq}}}{\mu_{\mathrm{N}}} = 31\,386;\ \mathrm{Pr} = \frac{\mu_{\mathrm{N}}c_{p,\mathrm{N}}}{\lambda_{\mathrm{N}}} = 0.76, \tag{B4}$$

where μ_{N} is the dynamic viscosity and λ_{N} is the thermal conductivity of the fluid, reported in Table B1 for different temperatures. The nitrogen phase change causes the Reynold number to rise from approximately 1862 in the liquid state to around 31 386 in the gas state, indicating a transition to turbulent flow. Fluid properties are evaluated at reference temperature corresponding to the average between the inlet, outlet and outer tube temperatures.

Table B1
Thermophysical properties of nitrogen at different temperature and atmospheric pressure.

Temperature T (°C)	Density ρ_{N} (kg/m^3)	Specific heat capacity $c_{p,\mathrm{N}}$ (J/(kg·K))	Dynamic viscosity μ_{N} (Pa·s)	Thermal conductivity λ_{N} (W/(m·K))	Phase
−196	806.6	2041.0	1.61×10^{-4}	0.145	Liquid
−196	4.556	1123.1	5.43×10^{-6}	0.007	Gas
−146	2.675	1054.1	8.69×10^{-6}	0.012	Gas
−131	2.386	1050.0	9.61×10^{-6}	0.013	Gas
−116	2.155	1047.3	1.05×10^{-5}	0.015	Gas
−101	1.964	1045.5	1.14×10^{-5}	0.016	Gas

Taking the heat absorbed by the liquid nitrogen (first term of Eq. (B5)) to be equal to the heat flux exchanged by convection on the outer surface of the pipes at temperature T_{s} and integrating along the pipe length L_{p}, it is possible to determine the evolution of the fluid temperature, assuming that only the outer tube of the freezing pipe exchanges heat with the surrounding environment:

$$\dot{m}_{\mathrm{N}}c_{p,\mathrm{N}}\mathrm{d}T = h_{\mathrm{N}}\left[T_{\mathrm{s}} - T_{\mathrm{f}}\left(x_{\mathrm{p}}\right)\right]\pi d_{\mathrm{p,eq}}\mathrm{d}x_{\mathrm{p}}, \tag{B5}$$

or

$$T_{\mathrm{f}}\left(x_{\mathrm{p}}\right) = T_{\mathrm{s}} - \left(T_{\mathrm{s}} - T_{\mathrm{f,in}}\right)\exp\left(-\frac{h_{\mathrm{N}}\pi d_{\mathrm{p,eq}}x_{\mathrm{p}}}{\dot{m}_{\mathrm{N}}c_{p,\mathrm{N}}}\right). \tag{B6}$$

T_{s} was evaluated by imposing an inlet and outlet temperatures of $T_{\mathrm{f,in}} = -196$ °C and $T_{\mathrm{f}}\left(L_{\mathrm{p}}\right) = -100$ °C, respectively. The pipe length is $L_{\mathrm{p}} =$ 33.5 and 32.0 m in the primary and secondary field trials.

Calculation of the thermal resistance in the heat conduction process around the freezing pipe

The thermal power $\dot{Q}$ per unit length in steady state conditions is defined as the ratio between the temperature change ΔT over the sum of all the time-independent ther-

mal resistances (R_i) of the different layers crossed, assumed in series. The thermal resistance of the system depends on the type of heat processes involved, thermal properties and thickness of the crossed layers. The processes considered in thermal resistance calculations are summarised in Table B2 and listed below:

(1) Thermal convection between the freezing coolant and the external tube of the pipe.
(2) Thermal conduction across the thickness of the outer tube of the pipe (characterised by a thermal conductivity $\lambda_p = 15\,W/(m \cdot K)$);
(3) Thermal conduction across the elastomer insulation, when present ($\lambda_{ins} = 0.03\,W/(m \cdot K)$);
(4) Thermal conduction across the mortar filling ($\lambda_m = 2.0\,W/(m \cdot K)$);
(5) Thermal conduction across the affected volume of the soil, subdivided in a frozen ($\lambda_{Tb1a}^{frozen} = 2.0\,W/(m \cdot K)$, $\lambda_{SG}^{frozen} = 3.5\,W/(m \cdot K)$) and unfrozen layer ($\lambda_{Tb1a}^{unfrozen} = 1.2\,W/(m \cdot K)$, $\lambda_{SG}^{unfrozen} = 2.0\,W/(m \cdot K)$).

Consistently with the assumptions made regarding the boundary condition of the field trial numerical model, the affected volume of soil was considered to extend 10 m far from the axis of the freezing pipe (with an affected soil diameter $d_s = 20$ m). The threshold between the frozen and the unfrozen volumes of soil, identified as the diameter $d_{s,f}$, was evaluated iteratively as the distance where the temperature crosses 0 °C.

Table B2
Thermal resistances of the heat processes between the freezing pipes and the surrounding layers.

Processes	Thermal resistance
(1) Convection between the coolant and the pipe	$R_{1,fluid} = \frac{1}{h_N \pi d_{p,eq}} = 0.4167\ \frac{mK}{W}$
(2) Conduction across the pipe tube	$R_{2,pipe} = \frac{1}{2\pi\lambda_p} \ln\left(\frac{d_{p,out}}{d_{p,out}-2t_{p,out}}\right) = 0.0011\ \frac{mK}{W}$
(3) Conduction across the insulation cover (if present)	$R_{3,insul} = \frac{1}{2\pi\lambda_{ins}} \ln\left(\frac{d_{p,out}+2t_i}{d_{p,out}}\right) = 3.2157\ \frac{mK}{W}$
(4) Conduction though the high conductivity cementitious mortar	$R_{4,mortar} = \frac{1}{2\pi\lambda_m} \ln\left(\frac{d_c}{d_{p,out}+2t_i}\right) = 0.0293\ \frac{mK}{W}$ ($R_{4,mortar} = 0.0712\ \frac{mK}{W}$ if there is not insulation)
(5a) Conduction through the volume of the frozen soil	$R_{5,Tb1a}^{frozen} = \frac{1}{2\pi\lambda_{Tb1a}^{frozen}} \ln\left(\frac{d_{s,f}}{d_c}\right) = 0.2519\ \frac{mK}{W}$, $R_{5,SG}^{frozen} = \frac{1}{2\pi\lambda_{SG}^{frozen}} \ln\left(\frac{d_{s,f}}{d_c}\right) = 0.1406\ \frac{mK}{W}$
(5b) Conduction through the volume of unfrozen soil	$R_{5,Tb1a}^{unfrozen} = \frac{1}{2\pi\lambda_{Tb1a}^{unfrozen}} \ln\left(\frac{d_s}{d_{s,f}}\right) = 0.2141\ \frac{mK}{W}$, $R_{5,SG}^{unfrozen} = \frac{1}{2\pi\lambda_{SG}^{unfrozen}} \ln\left(\frac{d_s}{d_{s,f}}\right) = 0.1343\ \frac{mK}{W}$
Total with insulation	$R_{SG} = 3.9463\ \frac{mK}{W}$, $R_{Tb1a} = 4.1374\ \frac{mK}{W}$
Total without insultation	$R_{SG} = 0.7789\ \frac{mK}{W}$, $R_{Tb1a} = 0.9700\ \frac{mK}{W}$

References

Afshani, A., & Akagi, H. (2015). Artificial ground freezing application in shield tunneling. *Japanese Geotechnical Society Special Publication, 3*(2), 71–75.

Alzoubi, M. A., Xu, M., Hassani, F. P., Poncet, S., & Sasmito, A. P. (2020). Artificial ground freezing: a review of thermal and hydraulic aspects. *Tunnelling and Underground Space Technology, 104*, 103534.

Andersland, O. B., & Ladanyi, B. (2003). *Frozen ground engineering*. John Wiley & Sons.

Armstrong, M. D., & Csathy, T. I. (1963). Frost design practice in Canada and discussion. *Highway Research Record, 33*, 170–201.

Arya, L. M., & Paris, J. F. (1981). A physicoempirical model to predict the soil moisture characteristic from particle-size distribution and bulk density data. *Soil Science Society of America Journal, 45*(6), 1023–1030.

Bear, J., & Cheng, A. H. D. (2010). *Modeling groundwater flow and contaminant transport, Vol. 23*, 89–103.

Braun, B., Shuster, J., & Burnham, E. (1979). Ground freezing for support of open excavations. *Engineering Geology, 13*(1–4), 429–453.

Casini, F., Guida, G., Restaini, A., & Celot, A. (2023). Water retention curve–based design method for the artificial ground freezing: the isarco river underpass tunnels within the brenner base tunnel project. *Journal of Geotechnical and Geoenvironmental Engineering, 149*(3), 04023007.

Chamberlain, E. J., & Gow, A. J. (1979). Effect of freezing and thawing on the permeability and structure of soils. In *Developments in Geotechnical Engineering* (Vol. 26, pp. 73–92). Elsevier.

Chang, D. K., & Lacy H.S. (2008). Artificial Ground Freezing in Geotechnical Engineering. *Proceedings of the 6th International Conference on Case Histories in Geotechnical Engineering*, Arlington, VA, August 11–16, 2008.

Colburn, A. P. (1964). A method of correlating forced convection heat-transfer data and a comparison with fluid friction. *International Journal of Heat and Mass Transfer, 7*(12), 1359–1384.

Comsol (2023). Introduction to Comsol Multiphysics®. https://www.comsol.com/ documentation, accessed on 06/09/2023.

Czaja, P., Kamiński, P., & Dyczko, A. (2020). *Polish experiences in handling water hazards during mine shaft sinking. mining techniques—past, present and future*. London: IntechOpen.

Frivik, P. E. (1981). State-of-the-art report. Ground freezing: thermal properties, modelling of processes and thermal design. *Engineering Geology, 18*(1–4), 115–133.

Gens, A. (2010). Soil–environment interactions in geotechnical engineering. *Géotechnique, 60*(1), 3–74.

Gioda, G., Locatelli, L., & Gallavresi, F. (1994). A numerical and experimental study of the artificial freezing of sand. *Canadian Geotechnical Journal, 31*(1), 1–11.

Guida, G., Vespo, V. S., Musso, G., & Della Vecchia, G. (2023). The role of hydraulic and thermal properties of soil on evaporation: a numerical insight. *Environmental Geotechnics*, 1–16.

Huang, S., Guo, Y., Liu, Y., Ke, L., & Liu, G. (2018). Study on the influence of water flow on temperature around freeze pipes and its distribution optimization during artificial ground freezing. *Applied Thermal Engineering, 135*, 435–445.

Jessberger, H. L. (1980). Theory and application of ground freezing in civil engineering. *Cold Regions Science and Technology, 3*(1), 3–27.

Laloui, L., & Rotta Loria, A. F. (2019). *Analysis and design of energy geostructures: theoretical essentials and practical application*. Chap: Academic Press (pp. 8).

Levin, L., Golovatyi, I., Zaitsev, A., Pugin, A., & Semin, M. (2021). Thermal monitoring of frozen wall thawing after artificial ground freezing: case study of petrikov potash mine. *Tunnelling and Underground Space Technology, 107*, 103685.

Li, Z., Chen, J., Sugimoto, M., & Mao, C. (2020). Thermal behaviour in cross-passage construction during artificial ground freezing: case of Harbin metro line. *Journal of Cold Regions Engineering, 34*(3), 05020002.

Meschke, G., Zhou, M. M., Abd Elrehim, M. Z., & Marwan, A. (2015). Computational modelling and optimization of artificial ground freezing in tunnelling. In *Computer Methods and Recent Advances in Geomechanics: Proceedings of the 14th International Conference of International Association for Computer Methods and Recent Advances in Geomechanics*, 2014 (IACMAG 2014) (pp. 1397-1402). Taylor & Francis Books Ltd.

Metro C S.c.p.A (2011a). Relazione Geotecnica. Tratta T3 Fori Imperiali-S. Giovanni. Progetto esecutivo.

Metro C S.c.p.A (2011b). Relazione Tecnica: commento e sintesi dei risultati del campo prova congelemento. Tratta T3 Fori Imperiali-S. Giovanni. Progetto esecutivo.

Nishimura, S., Gens, A., Olivella, S., & Jardine, R. J. (2009). THM-coupled finite element analysis of frozen soil: formulation and application. *Géotechnique, 59*(3), 159–171.

Noureldin A., Tabler H., Irvine-Halliday D., & Mintchev M.P. (2000). A New Borehole Surveying Technique for Horizontal Drilling Processes Using One Fiber Optic Gyroscope and Three Accelerometers. *IADC/SPE Drilling Conference*, New Orleans, Louisiana, February 2000.

Orth, W., & Müller, B. (2013). Temporary watertight connection of excavations to existing buildings and temporary waterproofing of structures by ground freezing. *Geomechanics and Tunnelling, 6*(3), 246–260.

Pahud, D. (2002). Geothermal energy and heat storage. Cannobio: SUPSI DCT LEEE. Scuola Universitaria Professionale della Svizzera Italiana.

Perrone, V. (1955). La Ferrovia Metropolitana di Roma. *Istituto Poligrafico dello Stato*.

Pimentel, E., Sres, A., & Anagnostou, G. (2012). Large-scale laboratory tests on artificial ground freezing under seepage-flow conditions. *Géotechnique, 62*(3), 227–241.

Russo, G., Corbo, A., Cavuoto, F., & Autuori, S. (2015). Artificial ground freezing to excavate a tunnel in sandy soil. Measurements and back analysis. *Tunnelling and Underground Space Technology, 50*, 226–238.

Sancho Calderon, D. (2022). *Improved engineering solutions for thermal design of artificial ground freezing*. [Doctoral dissertation, Universidad de Burgos].

Schmall, P. C., & Braun, B. (2006). Ground freezing—a viable and versatile construction technique. In *Current Practices in Cold Regions Engineering* (pp. 1–11). Orono, Maine, USA: American Society of Civil Engineers.

Schindler, U., Chrisopoulos, S., & Cudmani, R. (2023). Artificial ground freezing applications using an advanced elastic-viscoplastic model for frozen granular soils. *Cold Regions Science and Technology, 215*, 103964.

Schindler, U., Cudmani, R., Chrisopoulos, S., & Schünemann, A. (2024). Multi-stage creep behavior of frozen granular soils: experimental evidence and constitutive modeling. *Canadian Geotechnical Journal, 61*(1), 118–133.

Sopko, J. A. (2019). Design of ground freezing for cross passages and tunnel adits. In *Tunnels and Underground Cities. Engineering and Innovation Meet Archaeology, Architecture and Art* (pp. 1549–1558). CRC Press.

van Genuchten, M. T. (1980). A closed-form equation for predicting the hydraulic conductivity of unsaturated soils. *Soil Science Society of America journal, 44*(5), 892–898.

Viggiani, G.M.B., & Casini, F. (2015). Artificial ground freezing: from applications and case studies to fundamental research. In *Proceedings of the XVI European Conference on Soil Mechanics and Geotechnical Engineering*, ECSMGE 2015 (Vol. 1, pp. 65–92). ICE Publishing.

Viggiani, G. M. B., Losacco, N., Romani, E., & Sonnessa, A. (2022). Observed interaction between Line C of Roma underground and the Cloaca Maxima. In *Geotechnical Engineering for the Preservation of Monuments and Historic Sites III* (pp. 280–291). CRC Press.

Vitel, M., Rouabhi, A., Tijani, M., & Guérin, F. (2015). Modeling heat transfer between a freeze pipe and the surrounding ground during artificial ground freezing activities. *Computers and Geotechnics, 63*, 99–111.

Wilson, G. W. (1990). Soil evaporative fluxes for geotechnical engineering problems [Doctoral dissertation, University of Saskatchewan].

Zhao, Y. (2019, March). Influence of Frost Heave and Thaw Settlement of Connected Aisle on Tunnel Structure. In *Journal of Physics*: Conference Series, *1176*(4), 042027. IOP Publishing.

Zhelnin, M., Kostina, A., Prokhorov, A., Plekhov, O., Semin, M., & Levin, L. (2022). Coupled thermo-hydro-mechanical modeling of frost heave and water migration during artificial freezing of soils for mineshaft sinking. *Journal of Rock Mechanics and Geotechnical Engineering, 14*(2), 537–559.

Zhou, M. M., & Meschke, G. (2013). A three-phase thermo-hydro-mechanical finite element model for freezing soils. *International Journal for Numerical and Analytical Methods in Geomechanics, 37*(18), 3173–3193.